Electronic Supplementary Material (ESI) for Journal of Materials Chemistry A.

Supporting information

Synchronized Partial Metal Leaching and Amphoteric N−P Modification in MnO_2 and VO_x Pseudocapacitor beyond its Energy Density Limit

Experimental section

Material characterization: The structure, morphology, phases and surface chemistry of samples were investigated by filed-emission SEM (Hitachi S-4800) with EDS, TEM (HEOL JEM-2010), XRD (D8-advance with Cu Kα radiation source), XPS (AXIS-HSi), and Raman spectroscopy (Thermo DXR2xi). The BET surface area results were derived from the N_2 adsorption-desorption isotherms measured from BELSORP-mini. ICP (730 Series) was used to identify the ratio of Mn/Mo. X-ray absorption fine spectroscopy (XAFS) at the Mn K-edge was performed at beamline 7D of the Pohang Accelerator Laboratory (PAL) in Korea. The storage ring was operated at 3.0 GeV, with a ring current of 240–250 mA. A Si(1 1 1) double crystal monochromator was used to eliminate high-order harmonics by reducing the beamline intensity by 20–30%. K-edge energy calibration was used by the first maximum point of derivative of the absorption curve in the Mn metal reference foil. The K-edge XAS spectra of Mn were collected from the 7D beamline at PLSII. Reference Mn metal foil spectrum was used to calibrate the spectra of samples, followed by analysis using Athena software in Demeter package. The EXAFS was investigated by Fourier transformation of the post-edge lines from each metal, and the Fourier transformed spectra were plotted using an uncorrected distance scale. The k range of 3–10 and k-weight of 3 were used with a window range of 1.0 to 3 to fit EXAFS results by using Artemis software in Demeter package.[1] The agreement values (R factor) obtained between simulated and observed data were ~0.02 in all cases.

Preparation of Mo, F-doped MnO_2 (MMO): All reagents were purchased from Sigma-Aldrich. Carbon cloth (CC) (NARA Cell-Tech Corporation) was annealed at 500 ℃ for 2 h under air atmosphere to endow it with favorable hydrophilicity. First, 10 mL of mixed solution containing 20 mM $KMnO_4$, 6.25 mM $(NH_4)_6Mo_7O_{24}{\cdot}4H_2O$ and 78.8 mmol NH_4F was prepared. Then, the

solution was transferred to a Teflon-lined stainless steel autoclave, followed by dipping a piece of air-activated CC. The mixture was heat to 160 ℃ and maintained for 2 h in an electrical oven. After the autoclave cooled down to room temperature, MMO deposited on CC was washed with DI water at least three times and then dried in air. Mo-MnO_2 and F-doped MnO_2 were prepared by the same procedure without NH_4F and $(NH_4)_6Mo_7O_{24}{\cdot}4H_2O$, respectively. MnO_2 was synthesized the same method without any dopant. MMO-25 sample was prepared using 25 mmol $KMnO_4$, 7.81 mmol $(NH_4)_6Mo_7O_{24}{\cdot}4H_2O$ and 98.4 mmol NH_4F.

Preparation of activated MMO (A-MMO): A piece of MMO was placed in 10 mL of DI water in a Teflon-lined stainless steel autoclave, which was then heated to 140 ℃ and maintained for 2 h in an electrical oven. After the autoclave cooled down to room temperature, the A-MMO sample was washed with DI water and dried in air. A-MMO-25 was fabricated by treating MMO-25 using the same method. MnO_2 was activated by the same method to obtain A-MnO_2. To investigate the effect of hydrothermal activation time on the morphology of derived samples, controlled A-MMO-4 and A-MMO-6 samples were prepared by controlling hydrothermal time for 4 and 6 h, respectively. To investigate the effect of the activation temperature on the electrochemical performance, A-MMO-120 and A-MMO-160 were activated at 120 and 160 ℃, respectively. The mass loading of MMO, A-MMO and A-MMO-25 was measured to be 7.1, 6.4 and 8.5 mg cm^{-2}, respectively.

Preparation of N-doped graphene (NG): NG nanosheet was fabricated by one-step hydrothermal method.[2] Graphene oxide (GO) was first prepared by a Hummers' method. 40 mg of GO was dispersed in 10 mL of DI water and then sonicated for 30 min. Then, 0.8 g of $NH_4H_2PO_4$ was added to the above GO solution. The mixture was transferred into a Teflon-lined stainless steel autoclave and then heated to 180 °C and maintained for 2 h. Afterward, the resulting product was

washed with DI water three times and then freeze-dried. To prepare flexible NG-based electrode, a slurry was prepared by mixing NG with Super P and polyvinylidene fluoride with a mass ratio of 8:1:1 in N-methyl-2-pyrrolidone. The obtained slurry was carefully coated onto CC and dried at 60 °C in a vacuum oven overnight. The mass loading of NG on CC is around 14 mg cm^{-2}.

Preparation of N-VO_x, P-VO_x and N, P-VO_x: First, V_2O_5 nanowires were electrochemically deposited on CC at 0.7 V for 40 min, in which Pt and saturated calomel electrodes were applied as a counter electrode and a reference electrode, respectively. An aqueous solution containing 0.4 $_M$ vanadyl sulfate and 0.4 $_M$ ammonium acetate was used as the electrolyte. The electrodeposited V_2O_5 (E-V_2O_5) was washed with DI water three times and dried in air. To prepare a sample with high mass loading, the electrodeposition time was increased to 60 min, generating E-V_2O_5-60. Thereafter, 0.8 g of CH_4N_2O and 0.8 g of $NaH_2PO_2 \cdot H_2O$ were used as N and P precursors placed at two corundum crucibles, respectively. They were put at the upstream side in a tube furnace, while electrodeposited V_2O_5 was put at the downstream site. E-V_2O_5 was annealed in the presence of N and P precursors under Ar atmosphere to 400 ℃ with a heating rate of 2 ℃ min^{-1} and maintained for 2 h, leading to the formation of N, P-VO_x. The N, P-VO_x-60 sample was prepared by annealing E-V_2O_5-60 under the same condition. The V_2O_5 sample was fabricated by annealing E-V_2O_5 with the absence of N and P precursors. N-VO_x and P-VO_x samples were prepared by thermal treatment with the presence of either CH_4N_2O or $NaH_2PO_2 \cdot H_2O$, respectively. The mass loading of N, P-VO_x and N, P-VO_x-60 was measured to be 6.1 and 10.1 mg cm^{-2}, respectively.

lectrochemical measurement: CV, EIS, GCD curves and cycling stability of all electrodes were collected by CHI660E at a three-electrode system using 1 M Na_2SO_4 electrolyte. A platinum mesh and Ag/AgCl electrode were employed as a counter electrode as well as a reference electrode, respectively. The area of the working electrode was 1.0 cm^2. EIS data of electrodes were measured

within a frequency range of 0.1−100 kHz at an open-circuit AC with 5 mV amplitude. The flexible A-MMO//N, P-VO_x, A-MMO-25//N, P-VO_x-60, MMO//N, P-VO_x, and A-MMO//NG devices were assembled using gel electrolyte, and filter paper was applied as a separator. To prepare the gel electrolyte, 3 g PVA and 1.5 g Na_2SO_4 were added to 30 mL of DI water, which was then heated at 90 °C for at least 3 h under vigorous stirring to obtain PVA/Na_2SO_4 gel electrolyte. The total volume of the A-MMO//N, P-VO_x, A-MMO-25//N, P-VO_x-60, MMO//N, P-VO_x, and A-MMO//NG devices was measured to be 0.08 cm^3 (1 × 1 × 0.08), 0.09 cm^3 (1 × 1 × 0.09), 0.09 cm^3 (1 × 1 × 0.09), and 0.1 cm^3 (1 × 1 × 0.1), respectively.

The method for calculating electrochemical performance

The areal capacitance of flexible electrodes in a three-electrode test: The areal capacitance of all electrodes (C) was calculated according to Eq. S1:

$$C = \frac{I \times \Delta t}{A \times V} \quad \text{(Eq. S1)}$$

where C (mF cm^{-2}), A (cm^{-2}), I (mA) and Δt (s) are the areal capacitance, testing area, current density, and discharge time.

Charge balance of positive and negative electrodes for flexible SCs: Charges (Q) stored at the positive and negative electrodes are calculated via Eq. S2 and S3:

$$Q_- = C_{a,-} \times \Delta V \times A_- \quad \text{(Eq. S2)}$$

$$Q_+ = C_{a,+} \times \Delta V \times A_+ \quad \text{(Eq. S3)}$$

C, A, and ΔV refer to the areal capacitance, tested area, as well as potential window of the electrode, respectively. The value of Q_+ should be equal to that of $Q\_$ to maintain the charge balance of both electrodes. Therefore, their areal capacitance is described in Eq. S4:

$$\frac{C_{a,-}}{C_{a,+}} = \frac{\Delta V_+ \times A_+}{\Delta V_- \times A_-} \quad \text{(Eq. S4)}$$

ΔV_+ and ΔV_- of the positive and negative electrodes are 1.1 and 1.2 V, respectively. A_+ and A_- refer to the testing area of the positive and negative electrodes (1.0 cm^2).

The areal and volumetric capacitance of flexible SCs: The areal and volumetric capacitance of flexible SCs is calculated from Eq. S5 and S6:

$$C_a = \frac{I \times \Delta t}{\Delta V \times A} \quad \text{(Eq. S5)}$$

$$C_v = \frac{C_a}{V} \quad \text{(Eq. S6)}$$

C_a (mF cm^{-2}) and C_v (mF cm^{-3}) refer to the areal and volumetric capacitance of the SC. A and V represent the area (cm^2) and volume (cm^3) of the flexible SC. ΔV, Δt and I are denoted as the voltage window (V), discharging time (s), and current (mA).

Energy density and power density of flexible SCs: Based on Eq. S7 and S8, the volumetric energy density E (mWh cm^{-3}) as well as power density P (mW cm^{-3}) of the SC were calculated:

$$E = \frac{0.5 \times C_v \times (\Delta V)^2}{3.6} \quad \text{(Eq. S7)}$$

$$P = \frac{E \times 3600}{\Delta t} \quad \text{(Eq. S8)}$$

Computational method

All calculations were implemented using the Vienna Abinitio Simulation Package (VASP) code based on Density Functional Theory (DFT).[3,4] For the following calculations of properties, General gradient approximation (GGA) was used with the Perdew–Burke–Ernzerhof (PBE) functional[5] to describe the exchange-correlation potential. All structural models were entirely relaxed until the ionic Hellmann–Feynman forces were smaller than 0.001 eV/Å, the energy tolerances were less than 10^{-6} eV/atom. The interaction between core electrons and valence electrons were described using the frozen-core projector-augmented wave (PAW) method. Wave functions were expanded on a plane wave basis with high energy using plane-wave cutoff energy of 500 eV. The corresponding gamma-centered Monkhorst-Pack[6] electronic wavevector k-point samplings were denser than 0.2 $Å^{-1}$. The surfaces were created by starting from a bulk-relaxed structure of VO_2 and MnO_2. Specifically, the supercells of MnO_2 (001) were constructed by a 4×4 slab, while the supercell VO_2 (001) was modeled by a 3×2 slab with a vacuum layer of 15 Å. Correspondingly, the two Mo atoms and one F atom were doped into the lattices of MnO_2 (001) model. Note that a vacuum gap of 15 Å was added to prevent the interaction between slabs.

The adsorbed energy of adsorbed species marked as E_{ad} indicates the adsorbed capability of Na^+ ions. Adsorption formula can be defined as follows:

$$E_{ad} = E_{adsorbate/surface} - E_{adsorbate} - E_{surface}$$

Where $E_{adsorbate/surface}$, $E_{adsorbate}$, and $E_{surface}$ refer to the energy of adsorbate and surface, the energy of adsorbate, and the energy of surface.

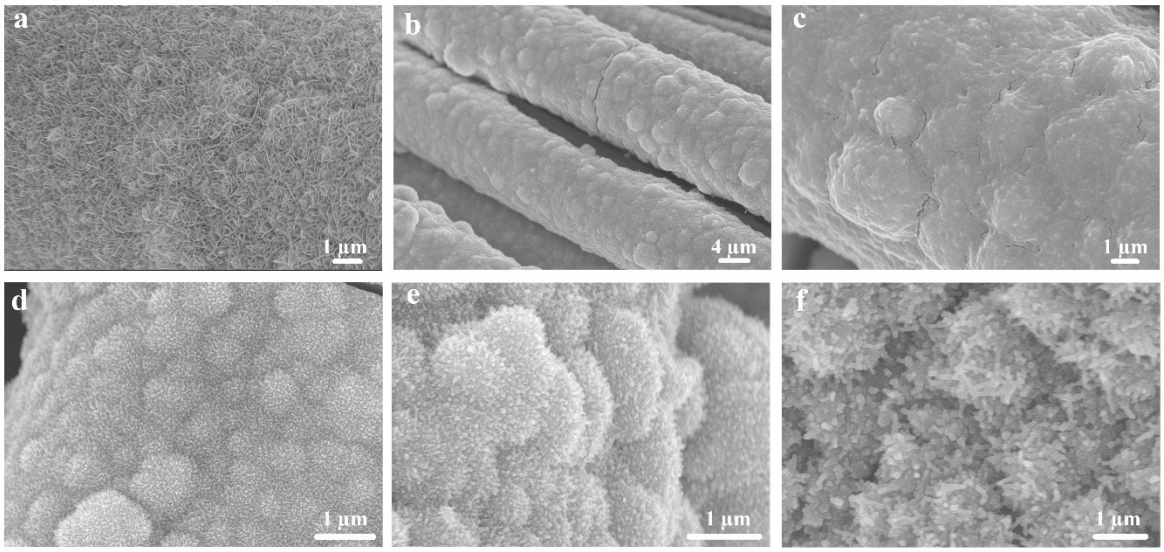

Fig. S1 SEM images of (a) F-doped MnO_2, (b-c) MMO, (d) A-MMO, (e) A-MMO-4, and (f) A-MMO-6 samples.

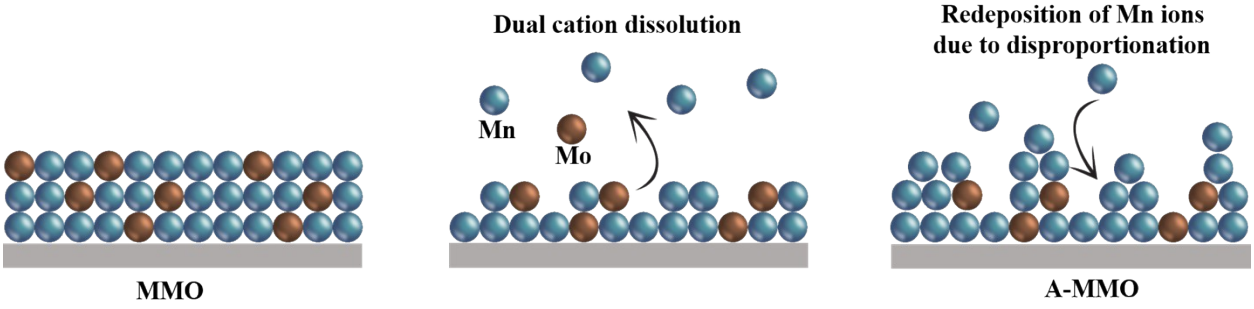

Fig. S2 Illustration of the cation dissolution and re-deposition of A-MMO during AHA. Grey color: CF substrate.

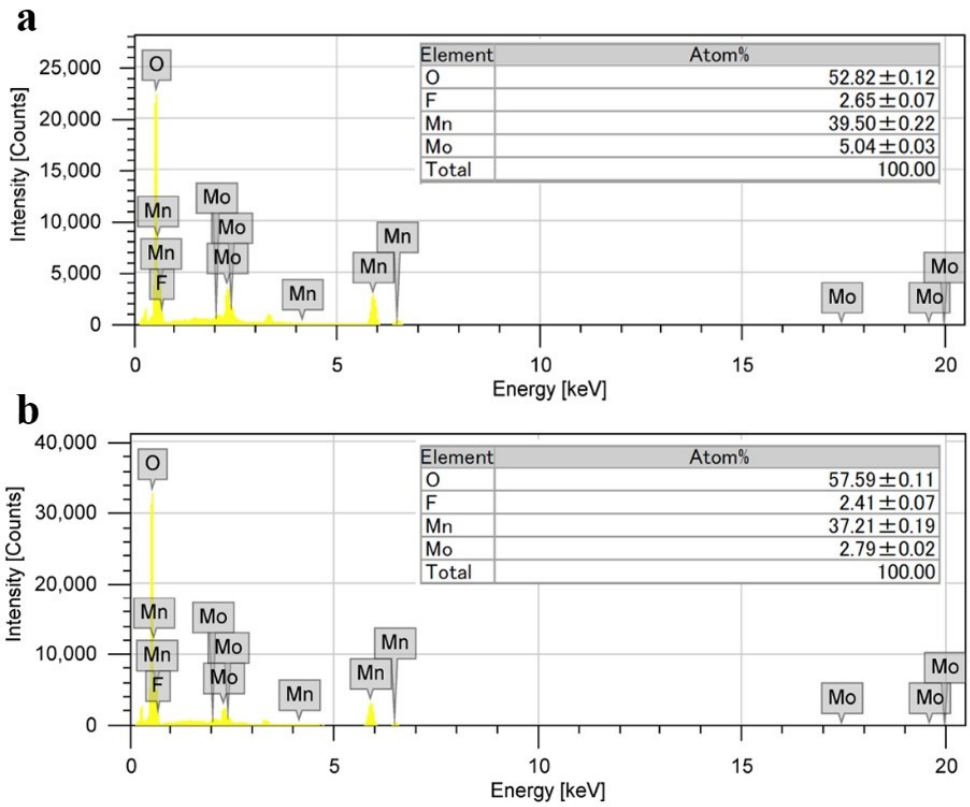

Fig. S3 The atomic percentage of elements from EDS mapping results in (a) MMO and (b) A-MMO.

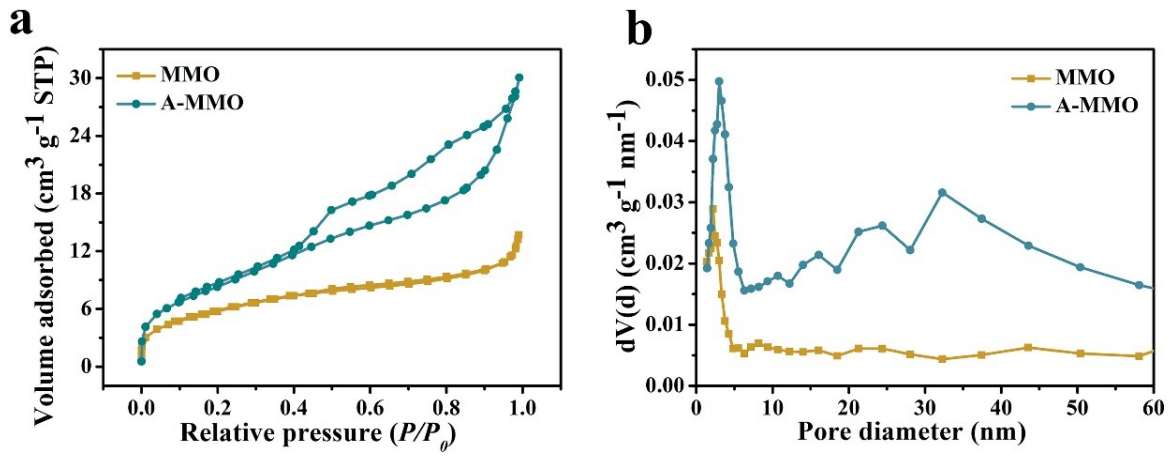

Fig. S4 (a) BET nitrogen adsorption-desorption isotherm curves and (b) Barrett-Joyner-Halenda (BJH) pore size distribution curves of MMO and A-MMO samples.

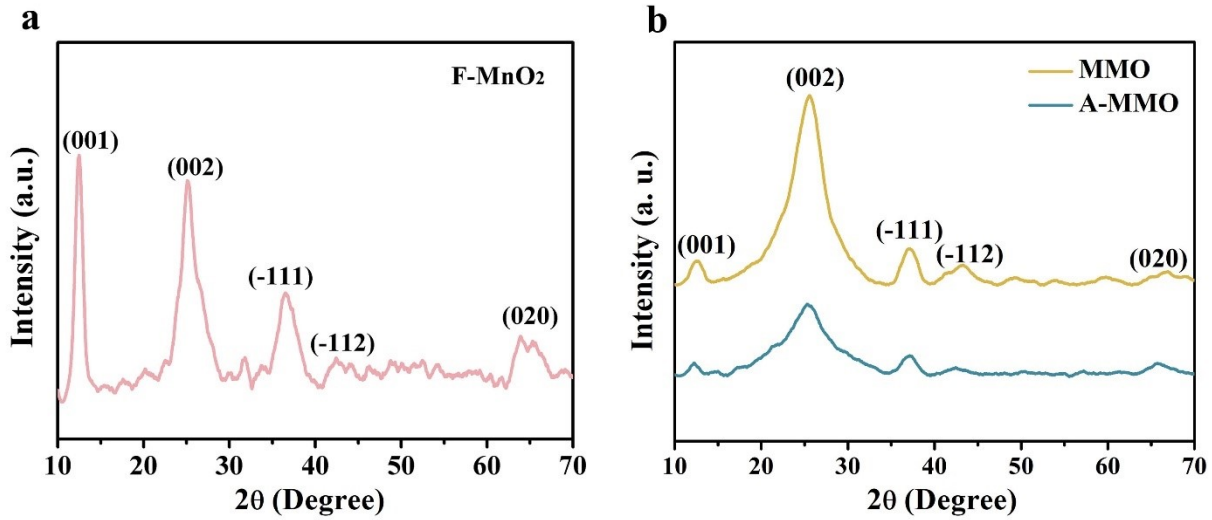

Fig. S5 XRD patterns of (a) F-doped MnO_2, and (b) MMO and A-MMO.

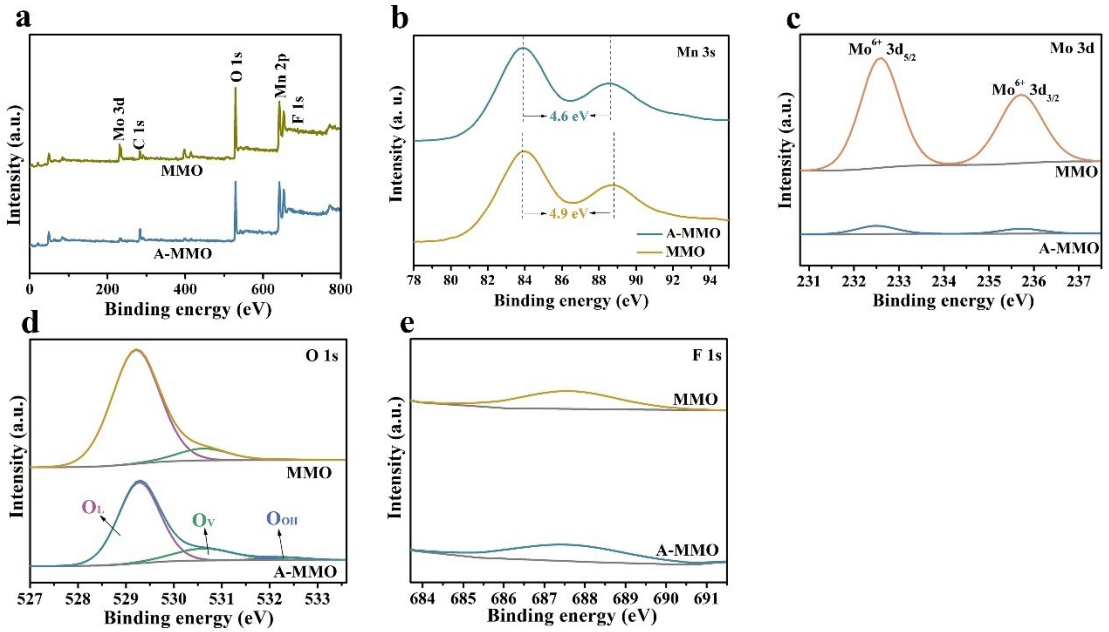

Fig. S6 (a) XPS survey spectrum, XPS spectra of (b) Mn 3s, (c) Mo 3d, (d) O 1s, and (e) F 1s of A-MMO and MMO samples.

Note to Fig. S6 The O 1s spectra of samples are split into three peaks at 529.3, 530.6, and 532.3 eV, corresponding to lattice oxygen (O_L), oxygen species with low coordination adsorbed on oxygen vacancies (O_V), and adsorbed water species (O_{OH}).[7]

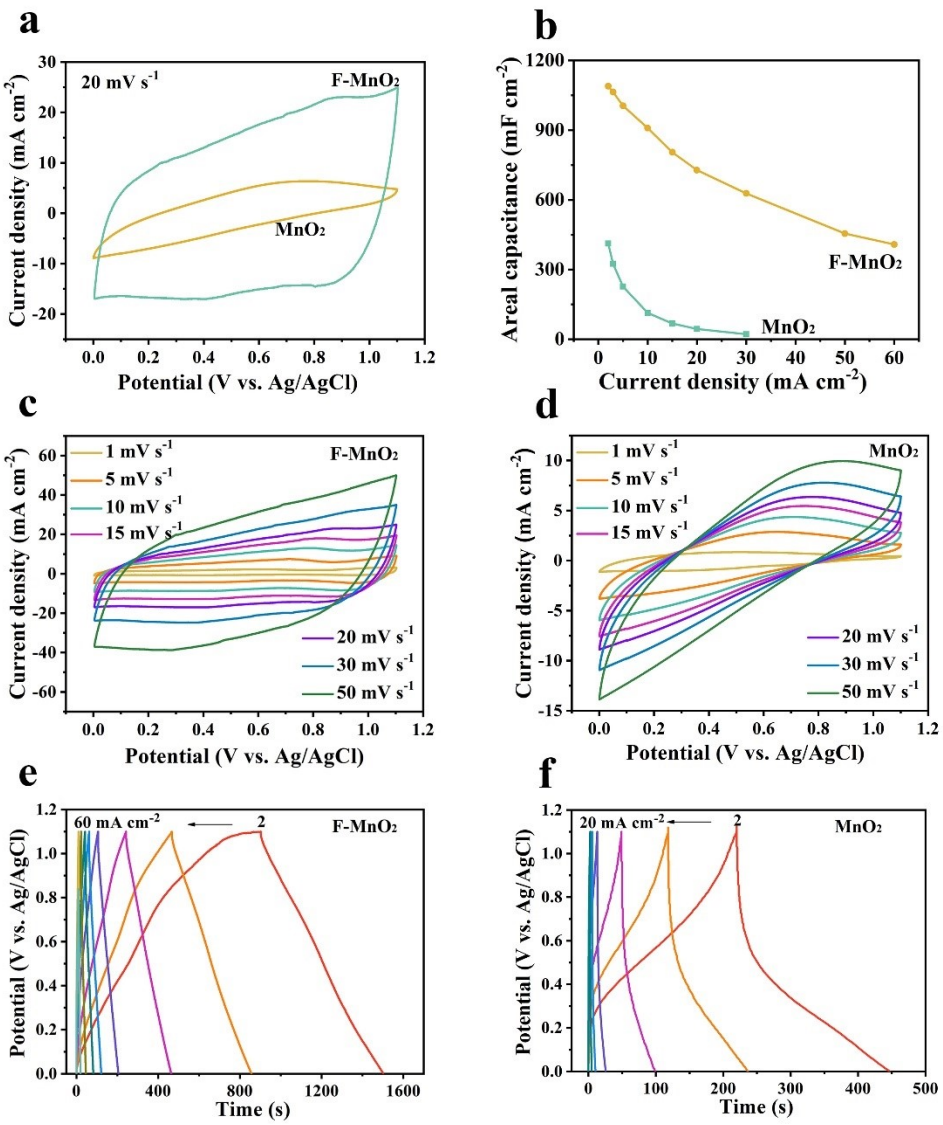

Fig. S7 (a) Comparison of CV curves of MnO_2 and F-MnO_2 at 20 mV s^{-1}. (b) Areal capacitances at different current densities of MnO_2 and F-MnO_2. CV curves of (c) MnO_2 and (d) F-MnO_2 at different scan rates from 1 to 50 mV s^{-1}. GCD curves of (e) MnO_2 and (f) F-MnO_2 at different current densities.

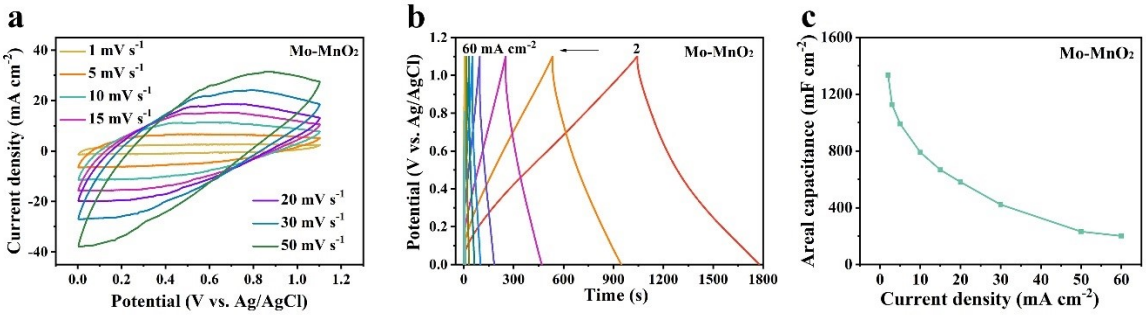

Fig. S8 (a) CV curves at different scan rates from 1 to 50 mV s^{-1}, (b) GCD curves of Mo-MnO_2.

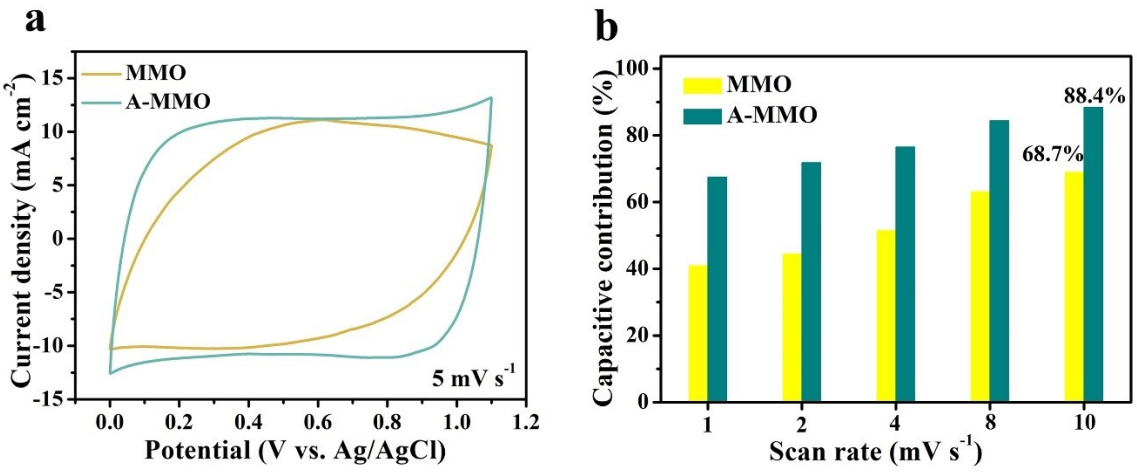

Figrue S9 (a) CV curves at 5 mV s^{-1}. (b) The percentage of capacitive contribution at various scan rates

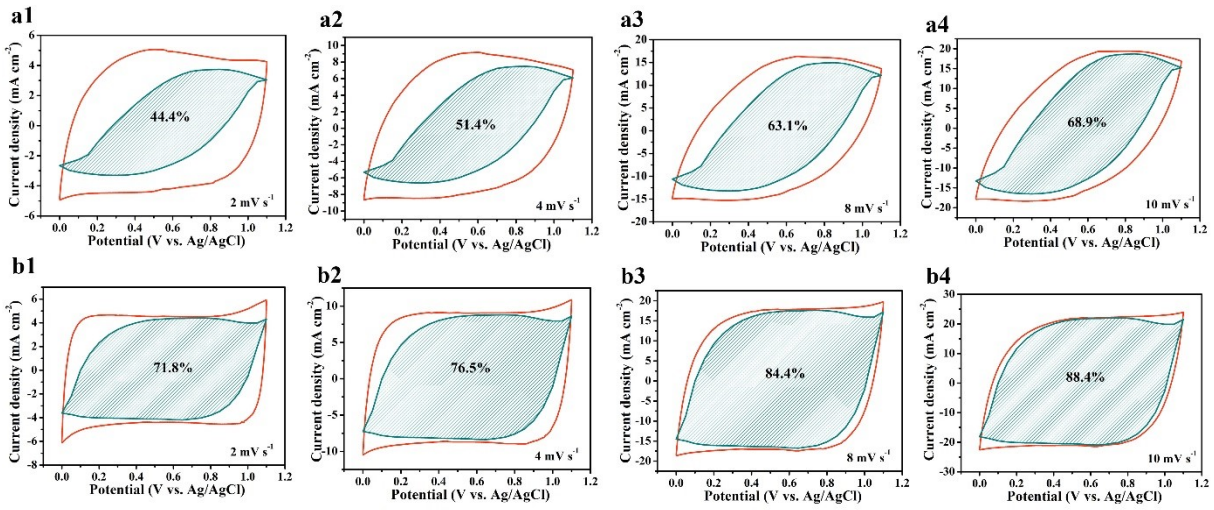

Fig. S10 Comparison of capacitive contribution (shaded area) in CV curves at 2, 4, 8, and 10 mV s^{-1} of (a1-a4) MMO, and (b1-b4) of A-MMO.

Note to Fig. S10 According to the Dunn's method,[8] charges stored in electrode materials can be divided to surface capacitive-controlled as well as diffusion-controlled processes. Based on Eq. S9 and S10, the relationship between the current density and scan rate in a CV profile at a specific potential is described as:

$$i(v) = k_1 v + k_2 v^{1/2} \quad \text{(Eq. S9)}$$

or

$$i(v)/v^{1/2} = k_1 v^{1/2} + k_2 \quad \text{(Eq. S10)}$$

where k_1 asnd k_2 refer to constants. i and v represent the current density and scan rate, respectively. k_1 and k_2 values can be derived from the slop and y-intercept at a given voltage a plot of $i/v^{1/2}$ vs. $v^{1/2}$, respectively. The capacitive- and diffusion-controlled processes are denoted as $k_1 v$ and $k_2 v^{1/2}$, respectively.

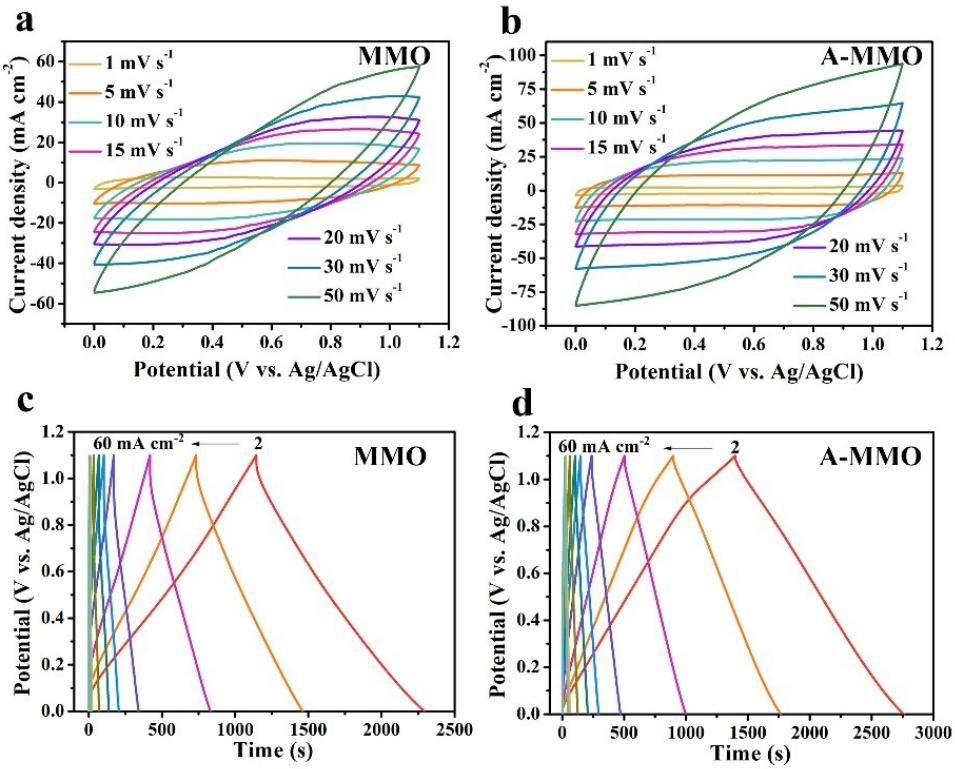

Fig. S11 CV curves of (a) MMO and (b) A-MMO at different scan rates from 1 to 50 mV s^{-1}. GCD curves of (c) MMO and (d) A-MMO at different current densities from 2 to 60 mA cm^{-2}.

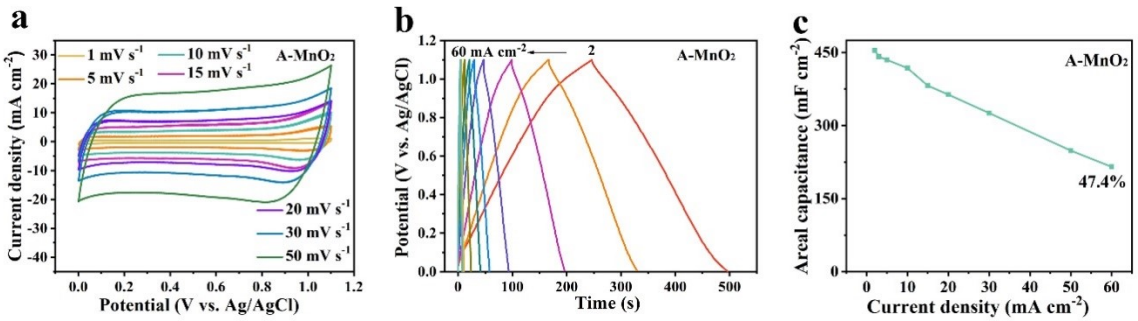

Fig. S12 (a) CV curves at different scan rates from 1 to 50 mV s^{-1}, (b) GCD curves of A-MnO_2.

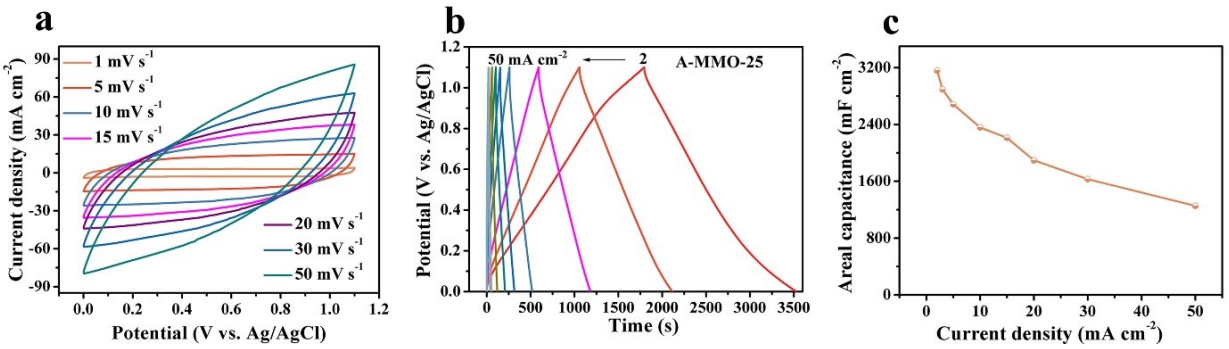

Fig. S13 (a) CV curves at different scan rates from 1 to 50 mV s^{-1}, (b) GCD curves at different current densities from 2 to 50 mA cm^{-2}, and (c) Areal capacitances at different current densities of A-MMO-25.

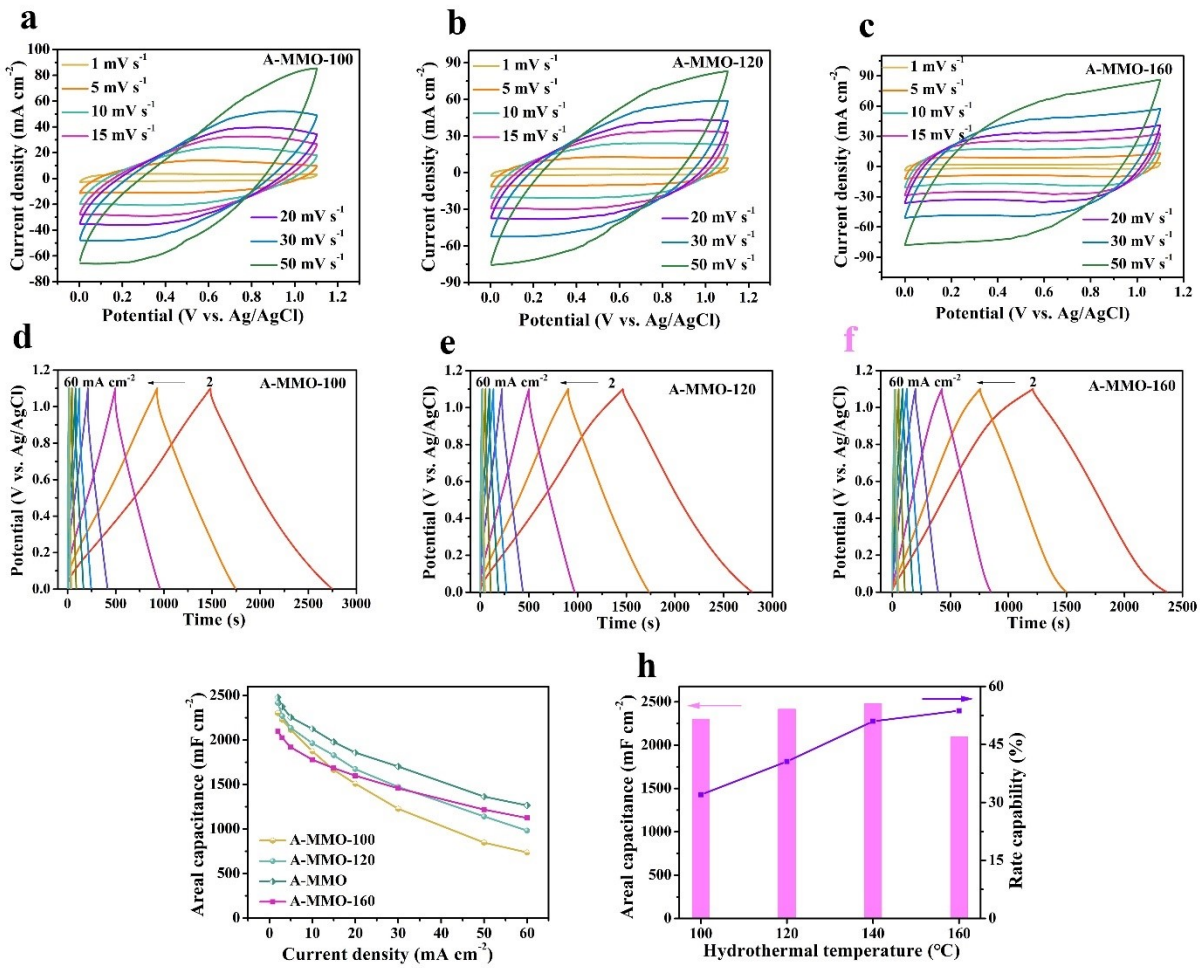

Fig. S14 CV curves of (a) A-MMO-100, (b) A-MMO-120, and (c) A-MMO-160 at different scan rates from 1 to 50 mV s^{-1}. GCD curves of (d) A-MMO-100, (e) A-MMO-120, and (f) A-MMO-160 at different current densities from 2 to 60 mA cm^{-2}. (g) Their areal capacitances at different current densities. (h) Comparison of areal capacitance of electrodes at 2 mA cm^{-2} and their rate capability at 60 mA cm^{-2}.

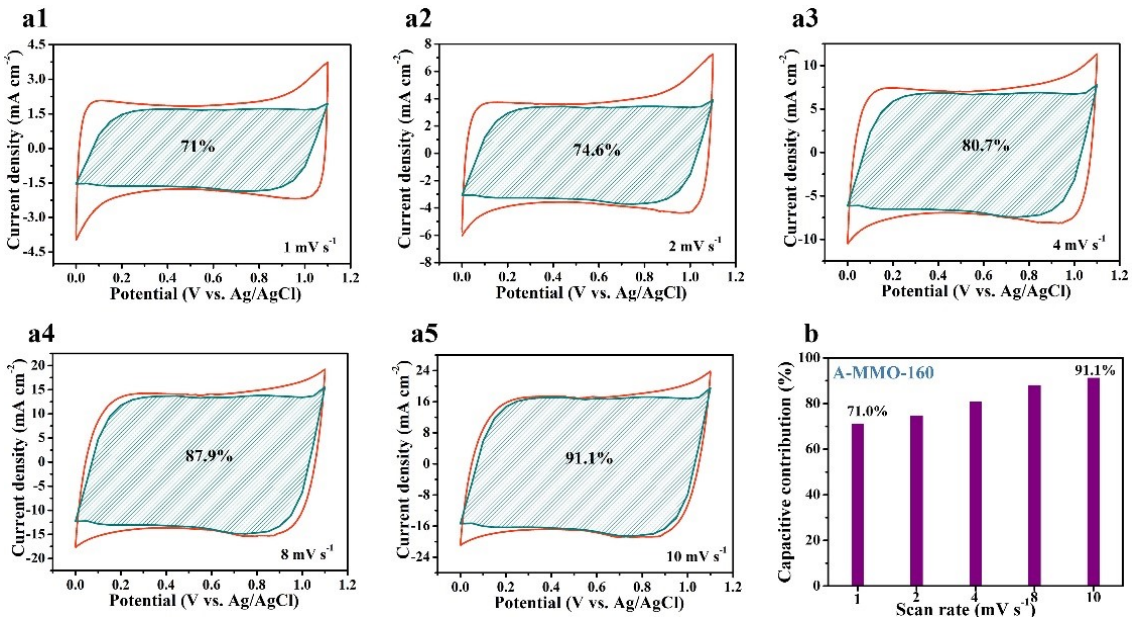

Fig. S15 (a1-a5) Comparison of capacitive contribution (shaded area) in CV curves of A-MMO-160 at 1, 2, 4, 8, and 10 mV s^{-1}. (b) Their percentage of capacitive contribution at various scan rates.

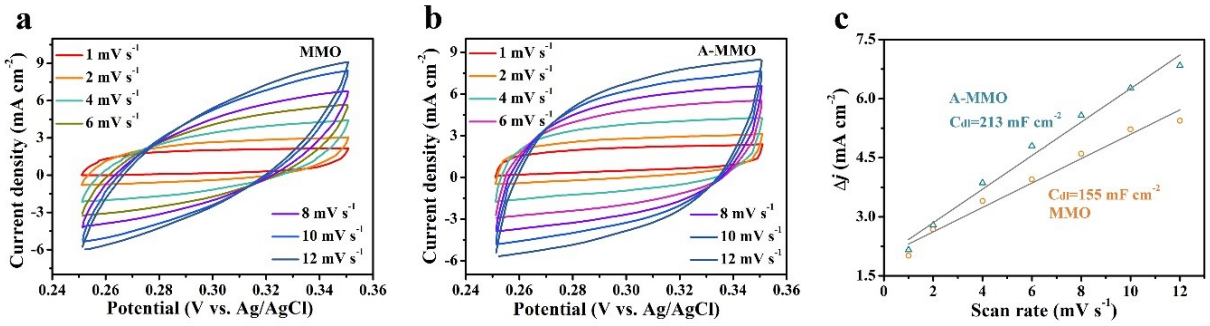

Fig. S16 CV curves of (a) MMO and (b) A-MMO in a potential window from 0.25 V to 0.35 V at different scan rates from 1 to 12 mV s^{-1}. (c) Charging current density differences Δj at 0.3 V as a function of different scan rates.

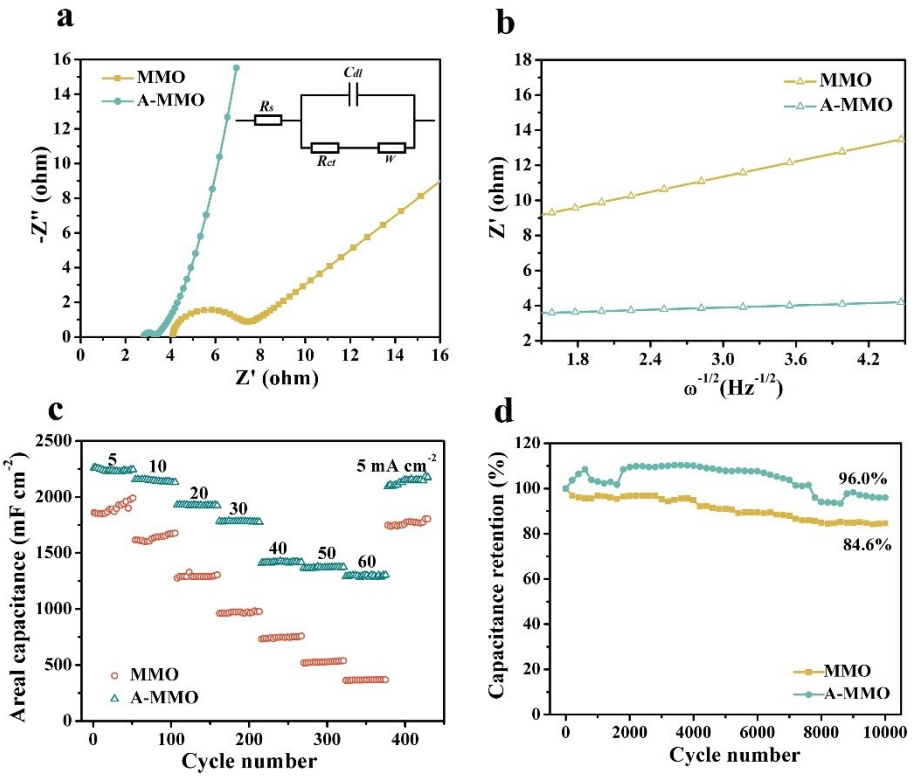

Fig. S17 (a) Nyquist plots (inset: a fitted equivalent circuit). (b) Relationship between Z' and $\omega^{-1/2}$. (c) Cycling stability at different current densities. (d) Long-term cycling test.

Note to Fig. S17 Electrochemical impedance spectroscopy (EIS) measurements of the MMO and A-MMO electrodes were used to study their electrochemical process. Warburg factors can be represented by the slope of the impedance (Z') vs. $\omega^{-1/2}$ plot in the Warburg region, and they are inversely proportional to the ion diffusion coefficient.[9] Fig. S14c shows the cycling stability of the two samples at different current densities from 5 to 60 mA cm^{-2}. MMO and A-MMO deliver average capacitances of 1898 and 2239 mF cm^{-2} at 5 mA cm^{-2}, respectively. When the current density was set back to 5 mA cm^{-2} after cycling at various current densities, 93.0% of the original capacitance in MMO was recovered, and 95.5% of that of A-MMO. Even after 10000 continuous cycles at 60 mA cm^{-2} (Fig. S14d), A-MMO retains 96.0% of the original capacitance and preserves an integrated structure, while 84.6% of the original capacitance of MMO is maintained.

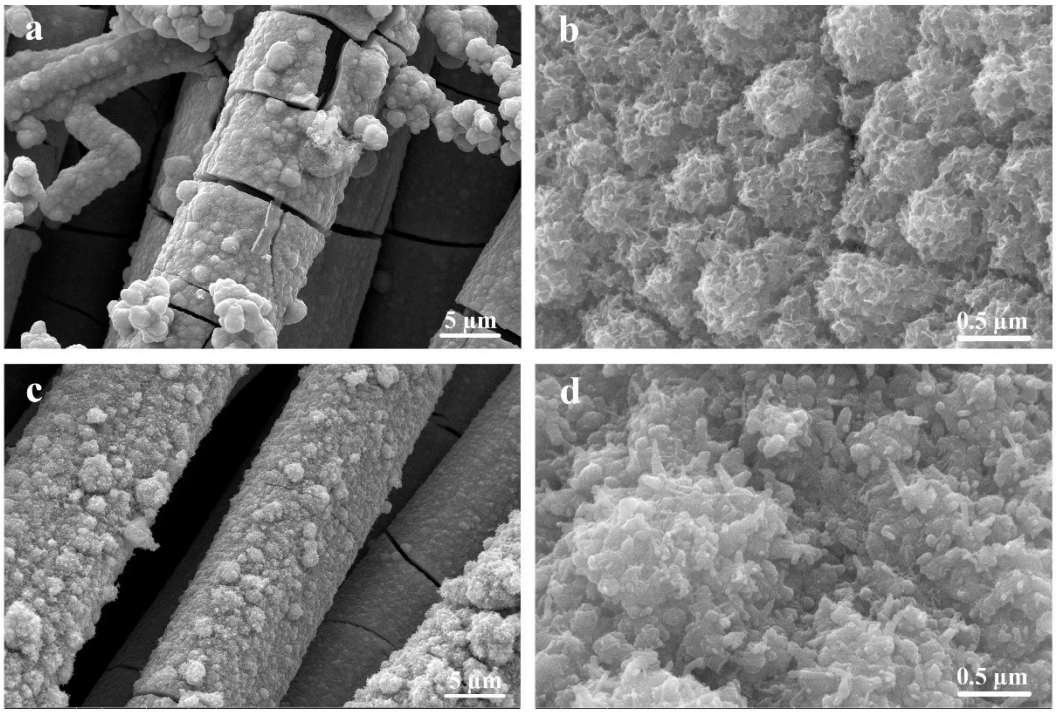

Fig. S18 SEM images of a, b) MMO and c, d) A-MMO after cycling.

Note to Fig. S17d and S18 The A-MMO sample shows an increased capacitance during the initial 800 cycles due to the gradual activation of bulk structure. The porous surface layer can perform as facile channels for ion penetration into the bulk material, which activates more active sites accessible for electrolyte ions during the initial cycling. However, MMO shows a smooth bulk structure where electrolyte ions hardly penetrate inside the material, which degrades its performance along cycling. As a result, MMO shows cracked structure with a porous nanosheet morphology, which is attributed to the repeated Na^+ insertion/extraction during the continuous charge/discharge process. A-MMO still demonstrates a rough surface with intact structure. As demonstrated by the *ex situ* XRD result, the cell volume of [MnO_6] could recovered after one charge/discharge process. CVAs can accommodate the volumetric change and thus mitigate the

structural strain during Na^+ insertion/extraction, ensuring highly reversible redox reactions and good cycling stability.

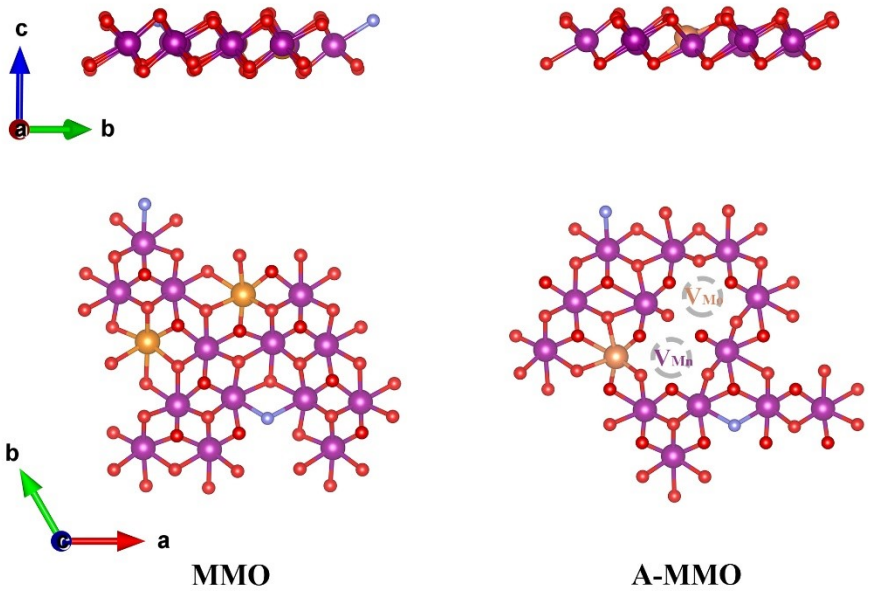

Fig. S19 Molecular structures of MMO and A-MMO.

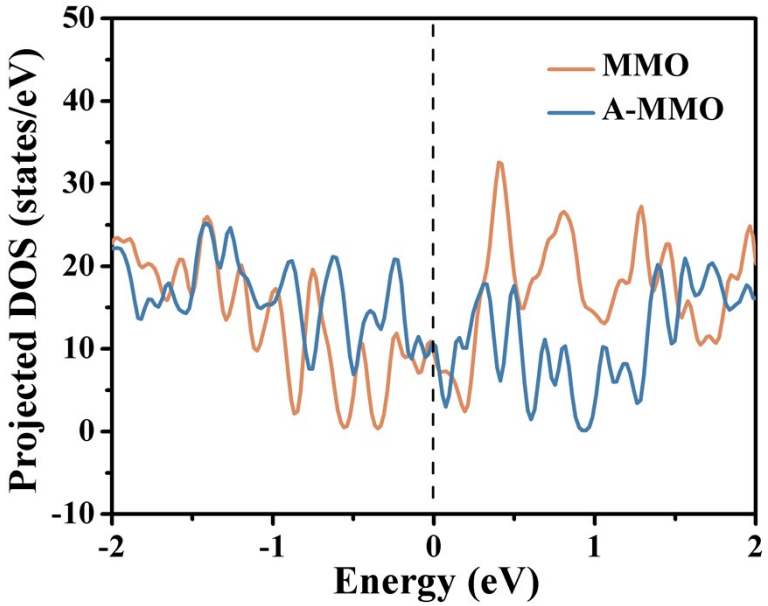

Fig. S20 PDOS of MMO and A-MMO.

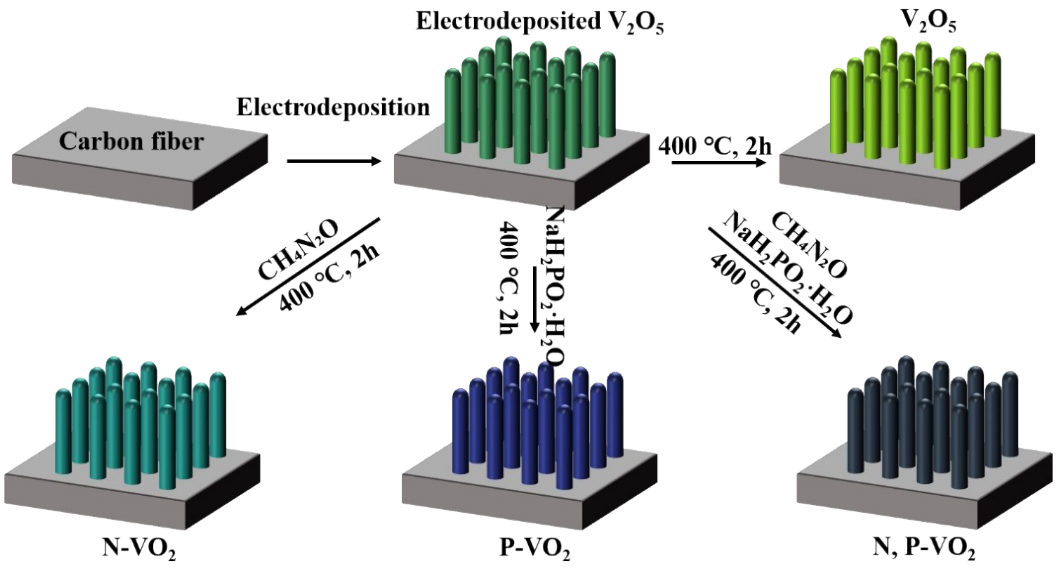

Fig. S21 Illustration of the process of preparing V_2O_5, N-VO_x, P-VO_x, N, P-VO_x.

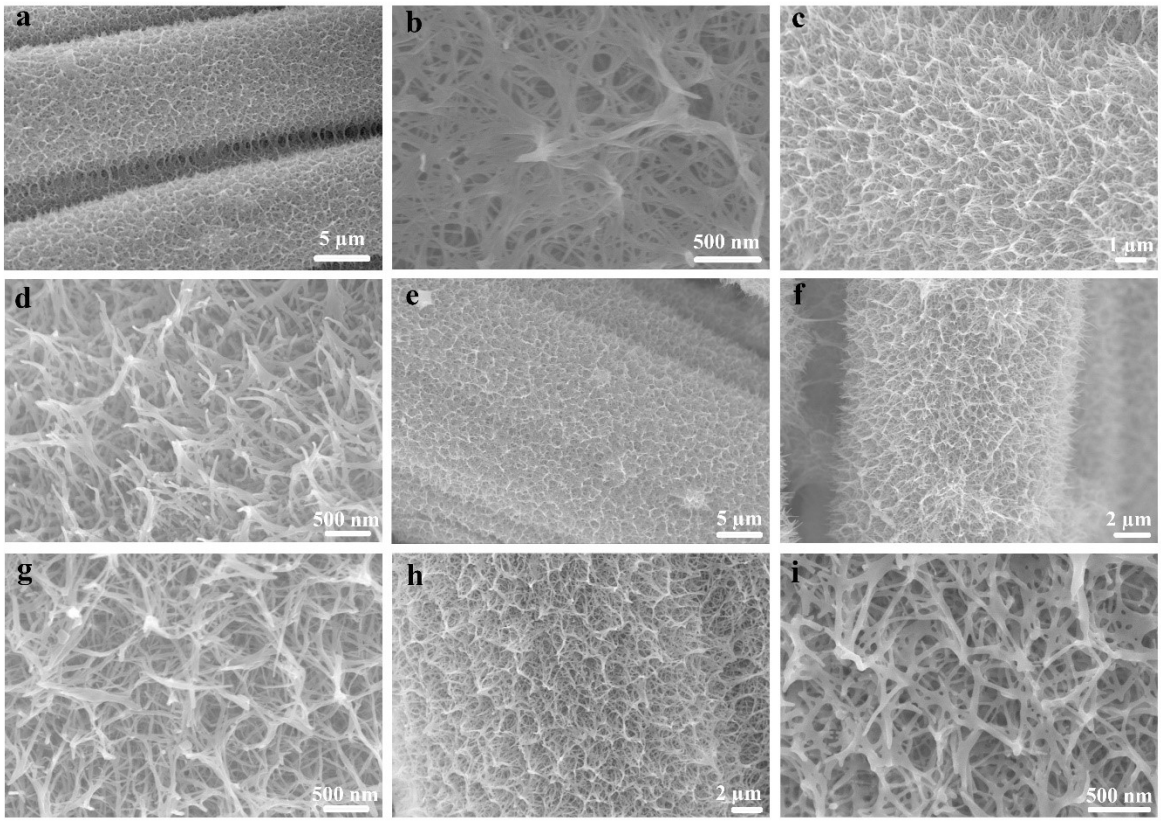

Fig. S22 SEM images of samples. (a, b) electrodeposited V_2O_5 on CFs. (c, d) V_2O_5. (e) N, P-VO_x. (f, g) N-VO_x. (h, i) P-VO_x.

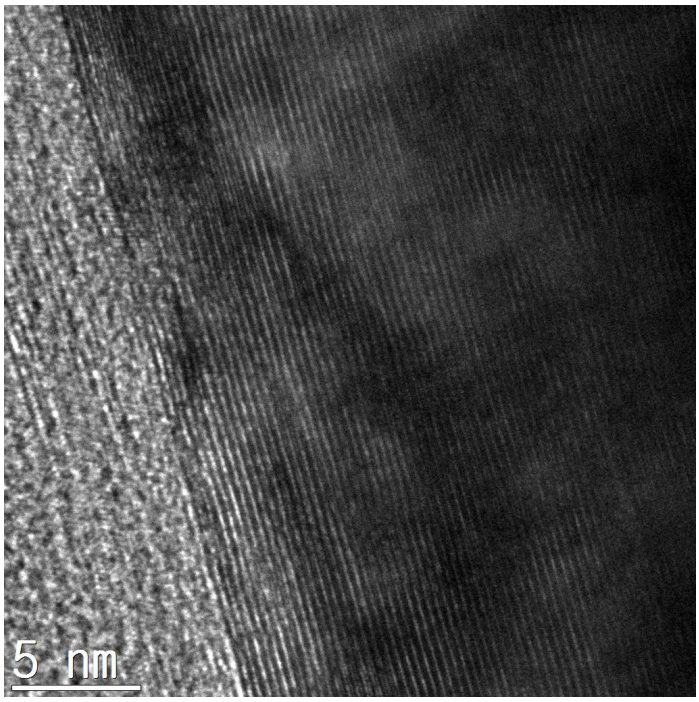

Fig. S23 HR-TEM imgae of V_2O_5.

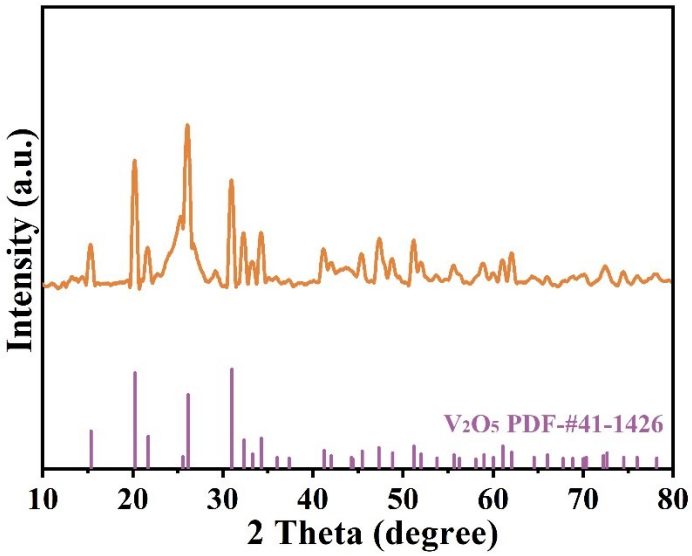

Fig. S24 XRD pattern of V_2O_5.

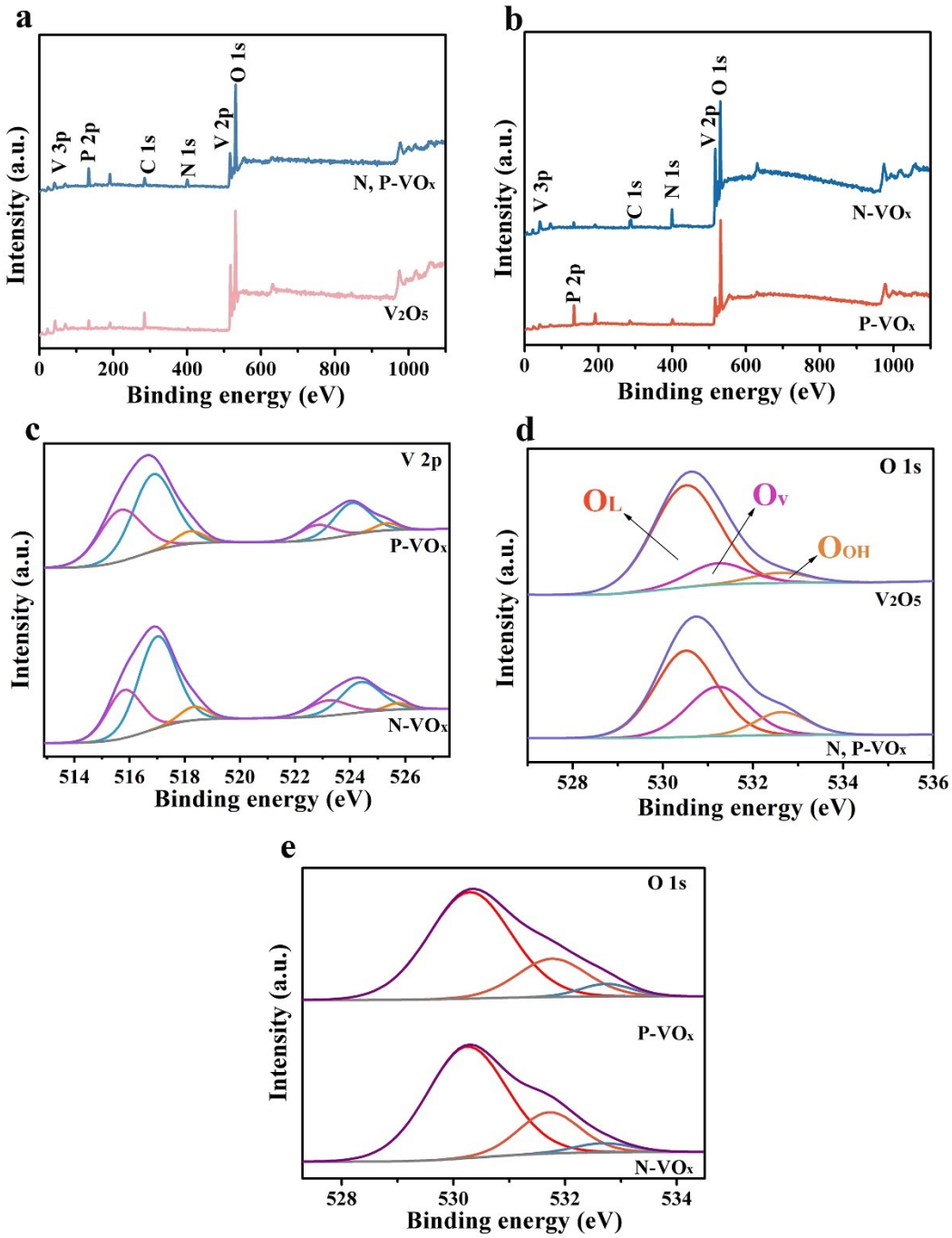

Fig. S25 XPS survey spectra of (a) V_2O_5 and N, P-VO_x, and (b) N-VO_x and P-VO_x. (c) XPS V 2p spectra of N-VO_x, and P-VO_x. XPS O 1s spectra of (d) V_2O_5, N, P-VO_x. (e) N-VO_x and P-VO_x.

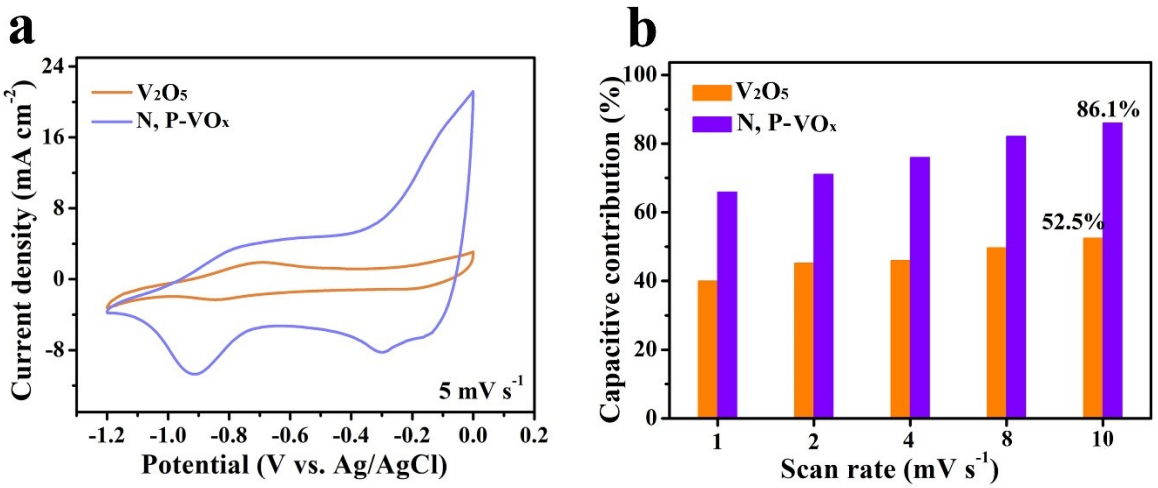

Figrue S26 (a) CV curves at 5 mV s^{-1}, and (b) the percentage of capacitive contribution at various scan rates of V_2O_5 and N, P-VO_x.

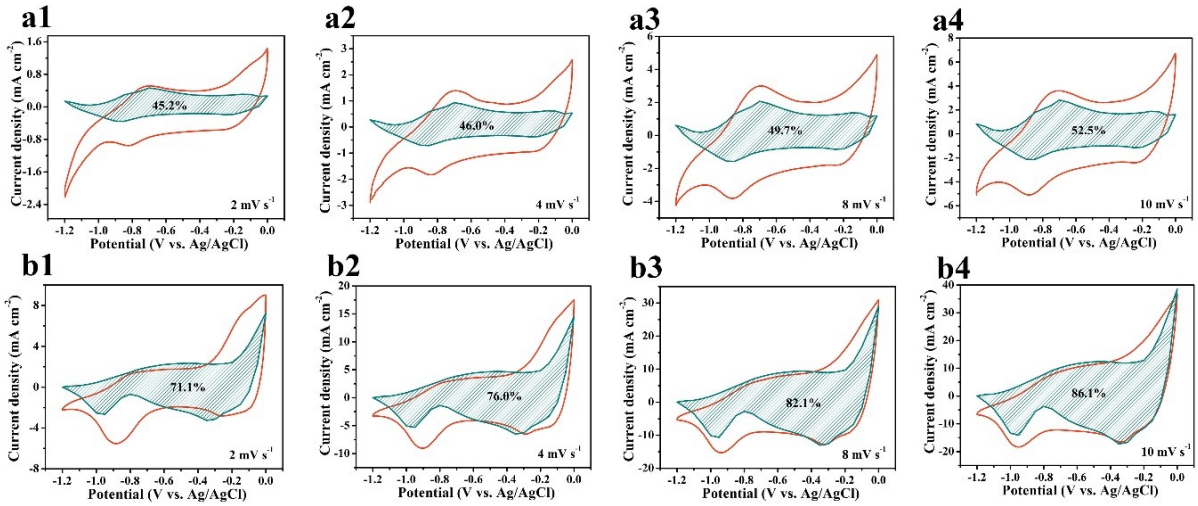

Fig. S27 Comparison of capacitive contribution (green shaded area) in CV curves at 2, 4, 8, and 10 mV s^{-1}. (a1-a4) of V_2O_5. (b1-b4) N, P-VO_x.

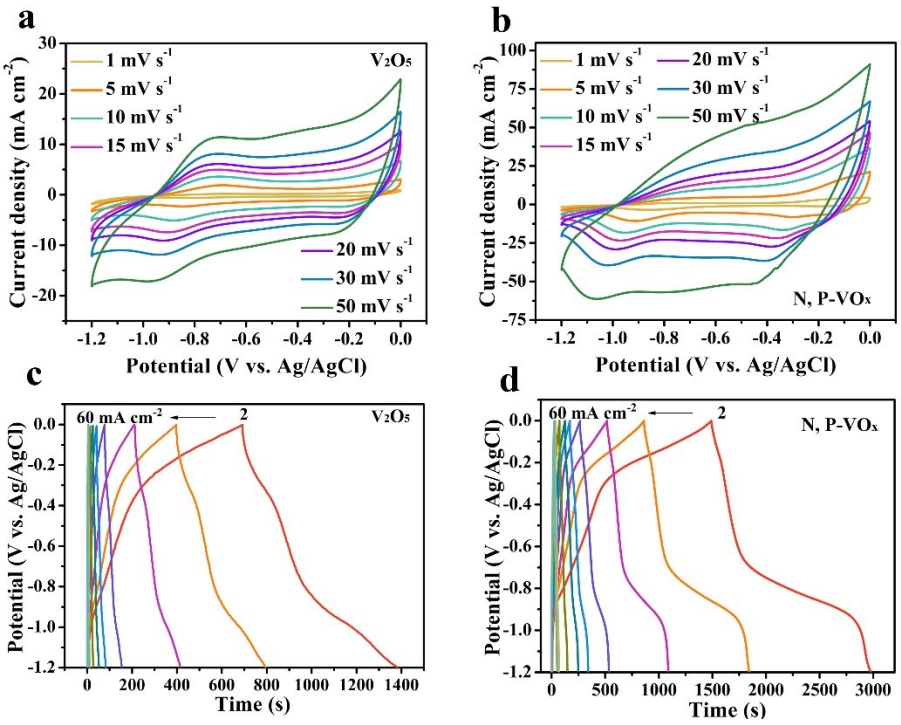

Fig. S28 CV curves of (a) V_2O_5 and (b) N, P-VO_x at different scan rates from 1 to 50 mV s^{-1}. GCD curves of (c) V_2O_5 and (d) N, P-VO_x at different current densities from 2 to 60 mA cm^{-2}.

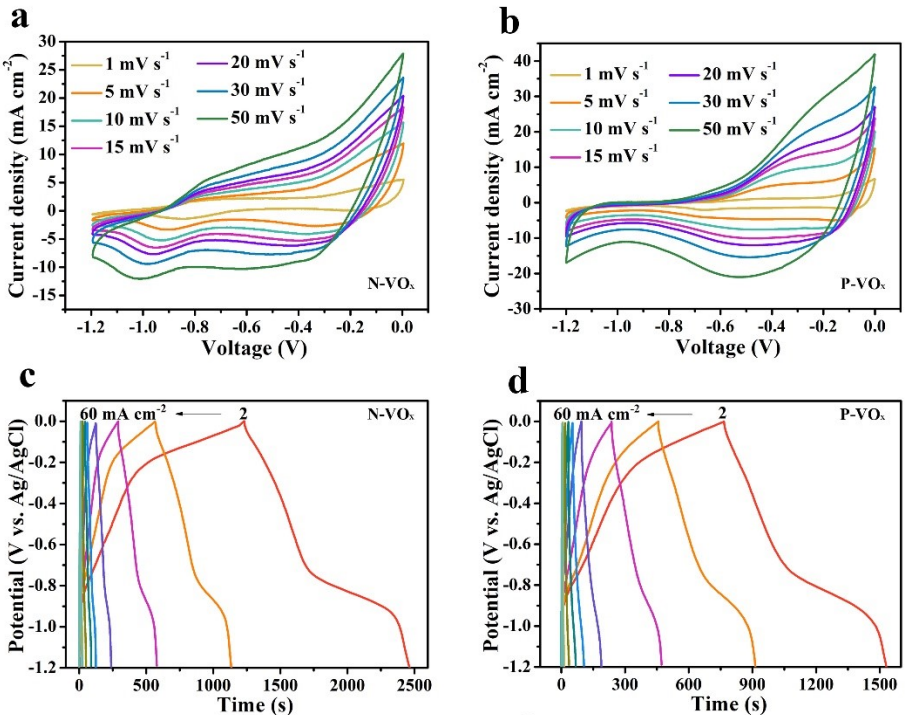

Fig. S29 CV curves of (a) N-VO_x and (b) P-VO_x at different scan rates from 1 to 50 mV s^{-1}. GCD curves of (c) N-VO_x and (d) P-VO_x at different current densities from 2 to 60 mA cm^{-2}.

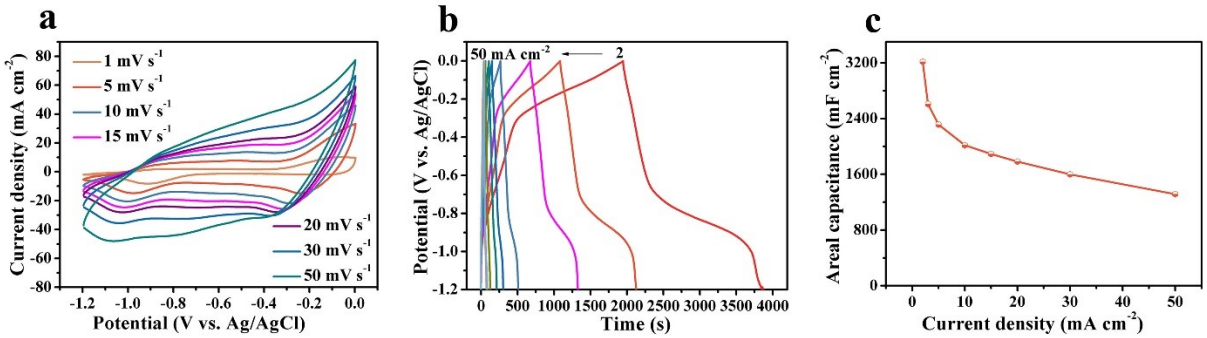

Fig. S30 (a) CV curves of N, P-VO_x-60 at different scan rates from 1 to 50 mV s^{-1}, (b) GCD curves at different current densities from 2 to 50 mA cm^{-2}, and (c) Their areal capacitances at different current densities.

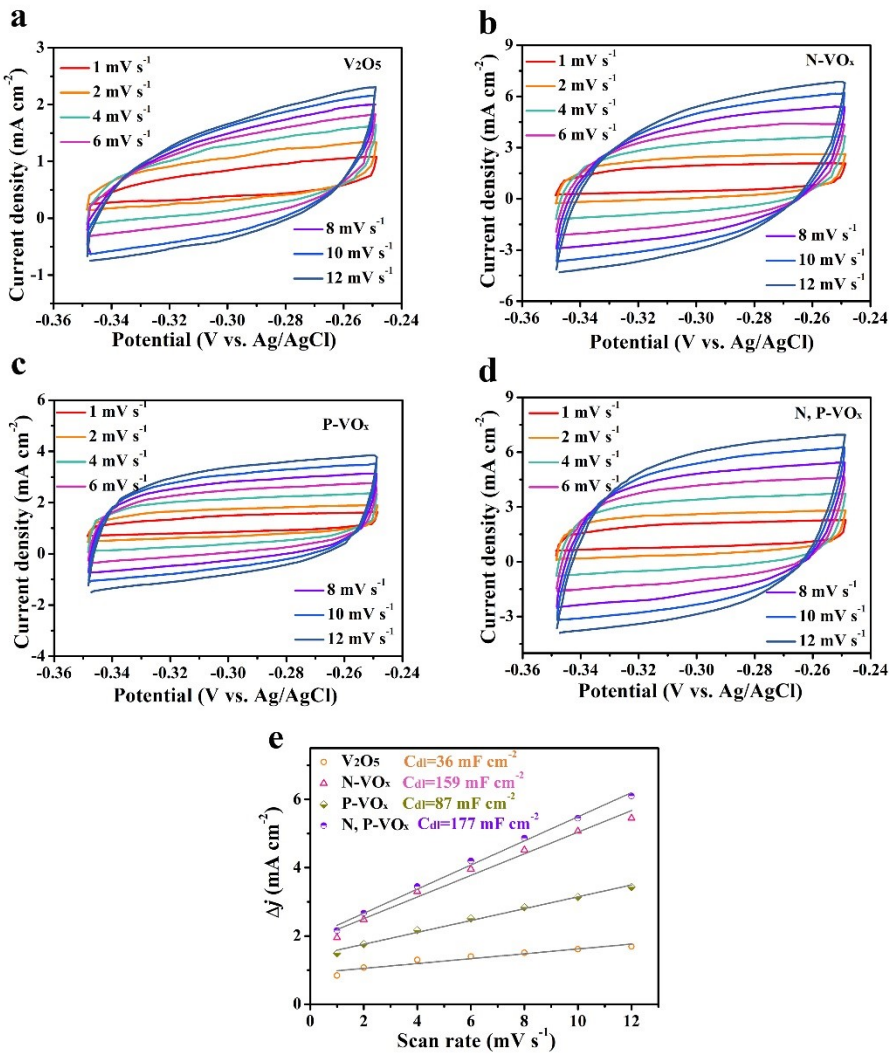

Fig. S31 CV curves of (a) V_2O_5, (b) N-VO_x, (c) P-VO_x, and (d) N, P-VO_x in a potential window from −0.35 V to −0.25 V at different scan rates from 1 to 12 mV s^{-1}. (e) Δj at −0.3 V as a function of different scan rates.

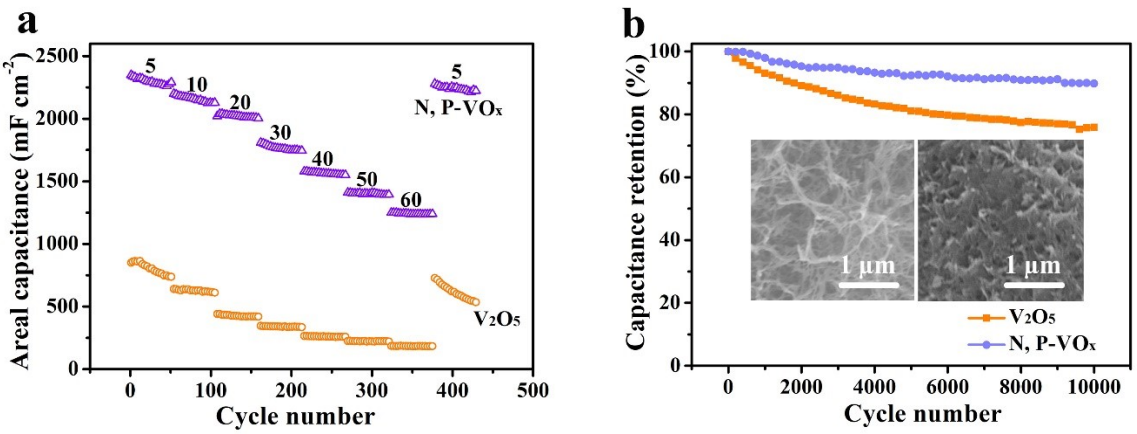

Fig. S32 (a) Cycling stability at different current densities. (b) Long-term cycling test and SEM images of N, P-VO_x and V_2O_5 after cycling, respectively (insets).

Note to Fig. S32 Fig. S28a shows V_2O_5 and N, P-VO_x deliver average capacitances of 803 and 2291 mF cm^{-2} at 5 mA cm^{-2}, respectively, and N, P-VO_x demonstrates better cycling stability than V_2O_5 at different current densities. When the current density was set back to 5 mA cm^{-2} after cycling at various current densities, 76.7% and 97.5% of the original capacitance were recovered, respectively. Moreover, N, P-VO_x, and V_2O_5 maintain 89.5% and 75.9% of the initial capacitance after 10000 cycles at 60 mA cm^{-2} (Fig. S28b).

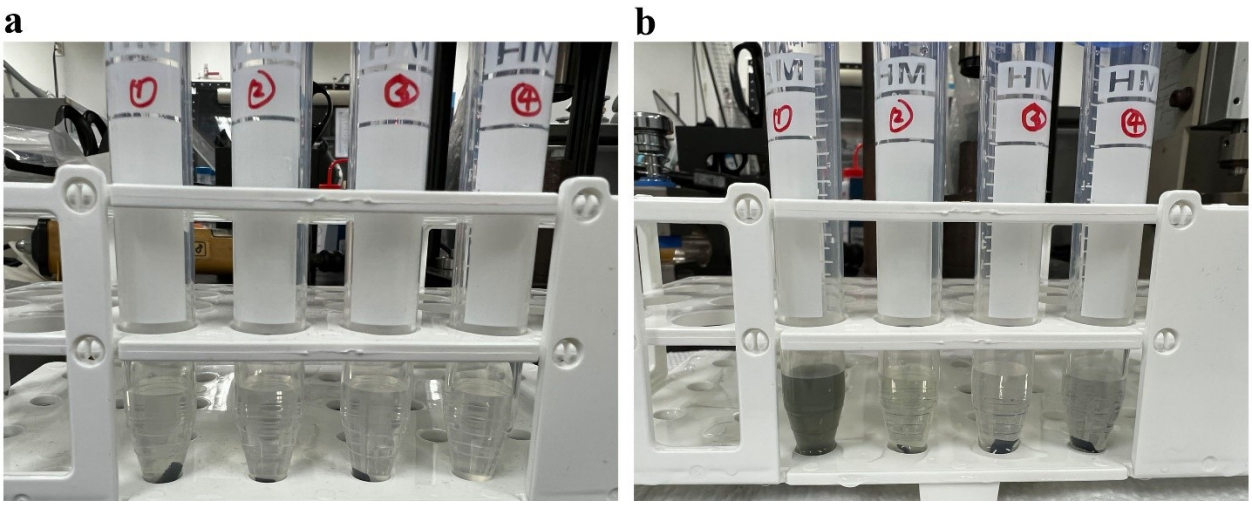

Fig. S33 Digital photographs of samples (a) before sonication, and (b) after sonication for 15 mins. Sample 1, 2, 3, and 4 marked in the photographs stand for V_2O_5, N-VO_x, P-VO_x, and N, P-VO_x, respectively.

Note to Fig. S33 Each sample with the same area was immersed in DI water. V_2O_5 shows serious dissolution after sonication compared with other samples.

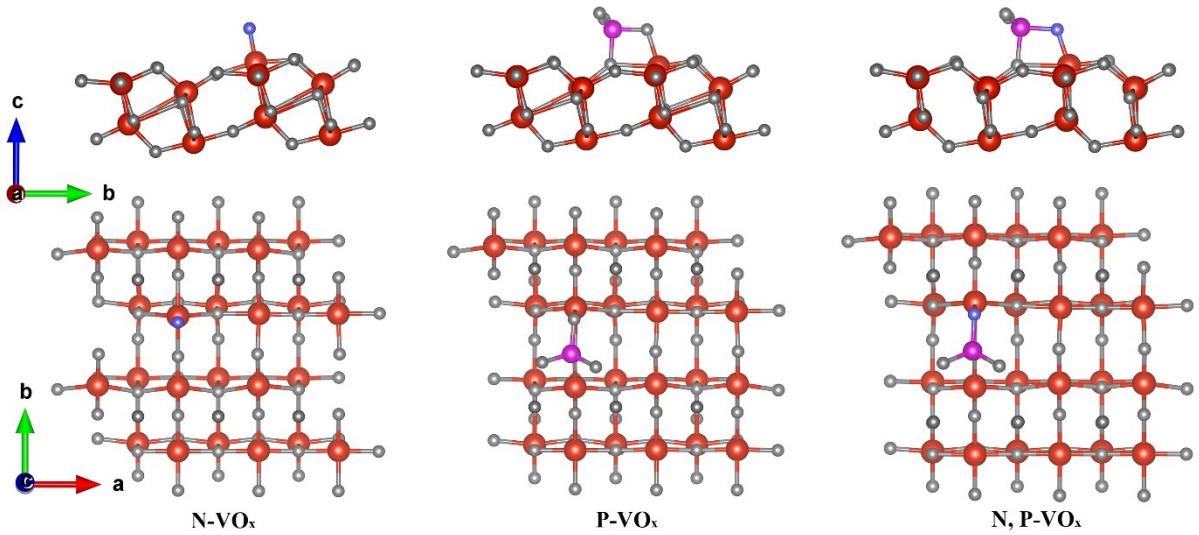

Fig. S34 Molecular structures of N-VO_x, P-VO_x, and N, P-VO_x.

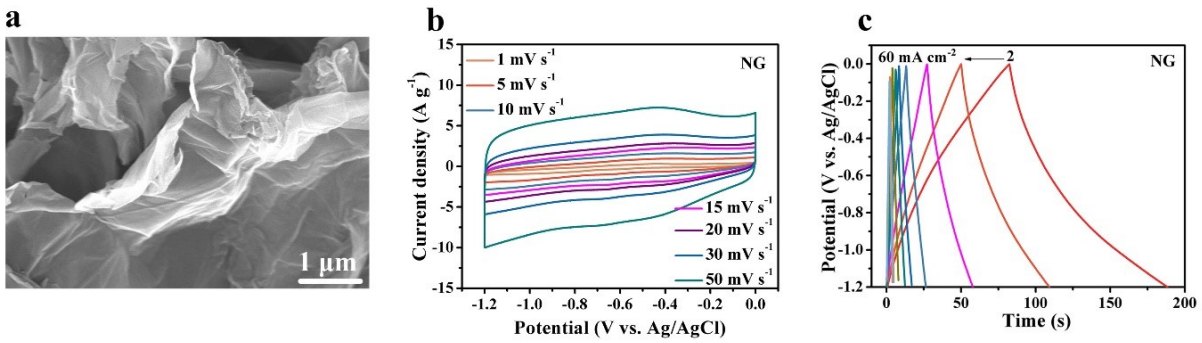

Fig. S35 (a) The SEM image, (b) CV curves of NG at different scan rates, and (c) GCD curves of NG at different current densities.

Note to Fig. S35 NG can deliver a specific capacitance of 177 F g^{-1} at 2 A g^{-1} and remain 45.2% of initial capacitance at 60 A g^{-1}.

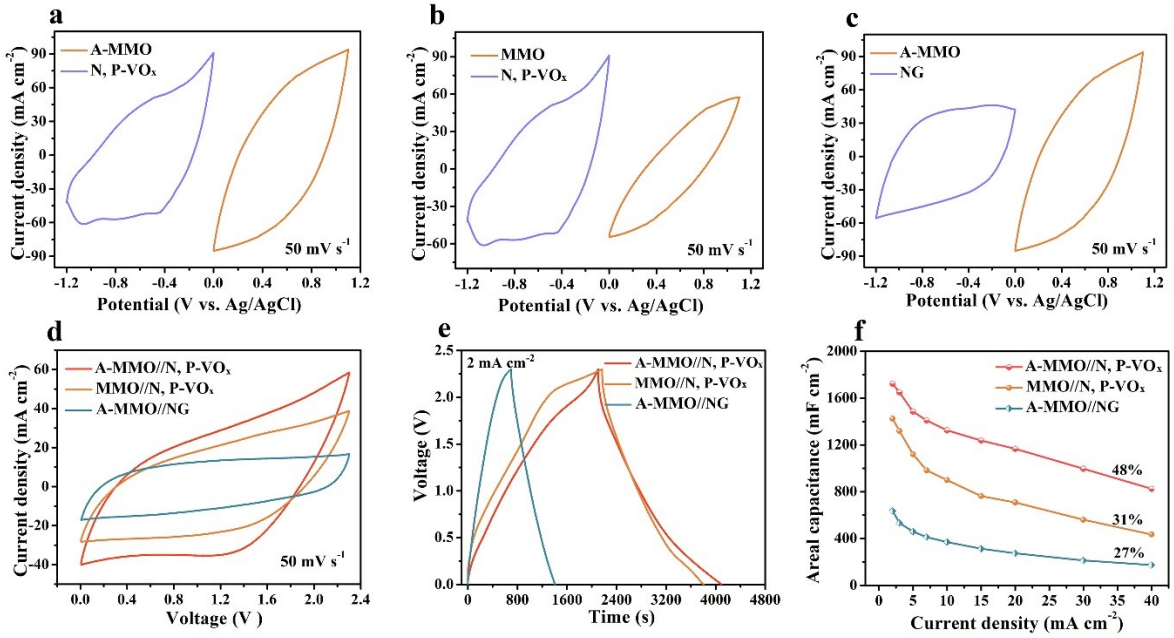

Fig. S36 Electrochemical performance of flexible quasi-solid-state A-MMO//N, P-VO_x, MMO//N, P-VO_x, A-MMO//NG SCs. (a-c) CV curve comparison at 5 mV s^{-1} of positive and negative electrodes of corresponding SCs. (d) CV curves at 5 mV s^{-1}. (e) GCD curves at 2 mA cm^{-2}. (f) Areal capacitances at different current densities from 2 to 40 mA cm^{-2}.

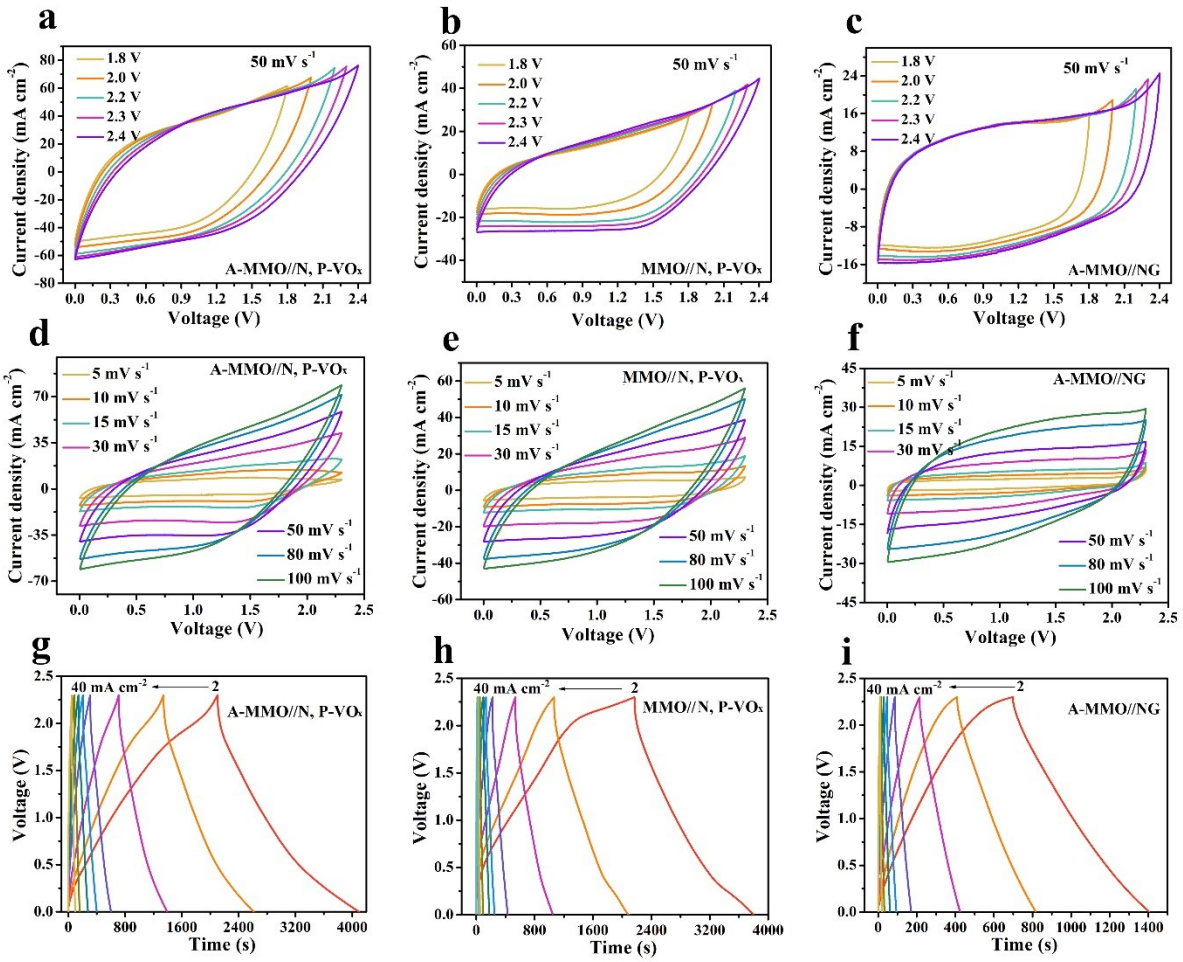

Fig. S37 (a-c) CV curves tested at different voltage windows. (d-f) CV curves at different scan rates. (g-i) GCD curves at different current densities of A-MMO//N, P-VO_x, MMO//N, P-VO_x, and A-MMO//NG devices.

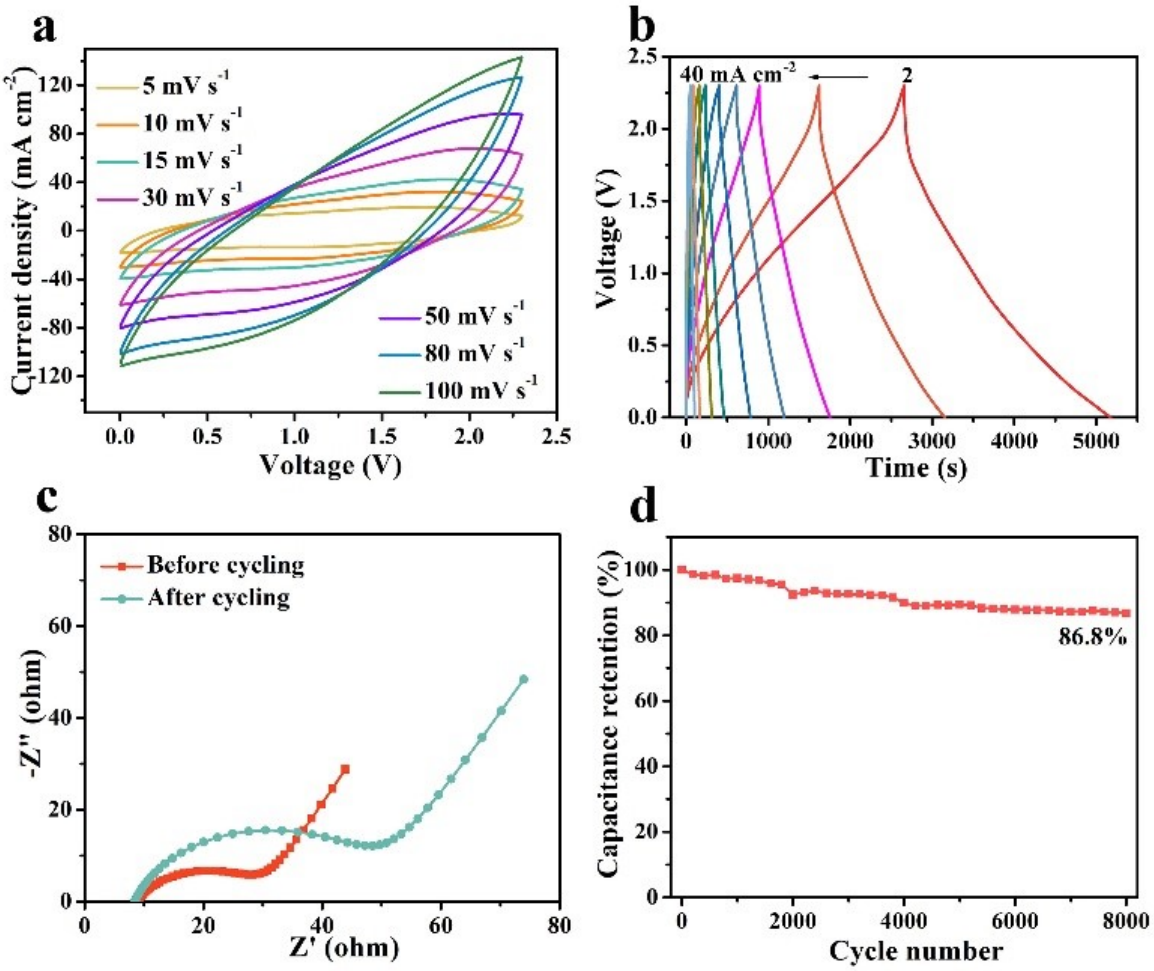

Fig. S38 The electrochemical performance of the A-MMO-25//N, P-VO_x-60 pseudocapacitor. (a) CV curves at different scan rates. (b) GCD curves at different current densities. (c) EIS plots before and after cycling. (d) Cycling stability.

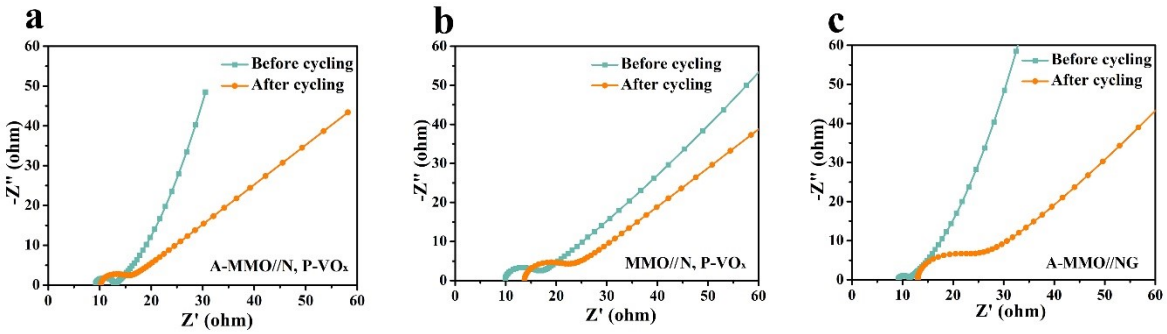

Fig. S39 EIS curves of (a) A-MMO//N, P-VO_x, (b) MMO//N, P-VO_x, and (c) A-MMO//NG devices before and after cycling.

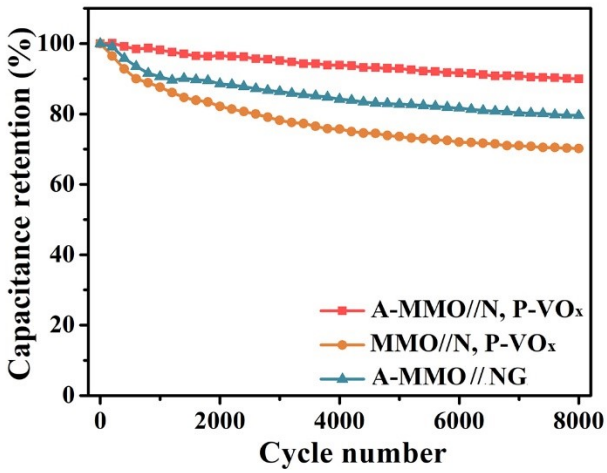

Fig. S40 Cycling stability of A-MMO//N, P-VO_x, MMO//N, P-VO_x and A-MMO//NG devices.

Table S1. Values of the amplitude reduction factors (S_0^2), coordination numbers (CN), energy shift (E_0), Debye-Waller factors (σ^2), interatomic distance (R) and R factor obtained from Mn K-edge FT-EXAFS spectra of MMO and A-MMO

Samples	Bonds	S_0^2	CN	σ^2 (Å^2)	E_0 (eV)	R (Å)	R factor
MMO	Mn-O	0.8	4.51	0.00687	-2.277	1.884	0.0179
	Mn-Mn	0.8	3.27	0.00893	-2.277	2.88	
A-MMO	Mn-O	0.8	4.33	0.00587	-2.244	1.887	0.0228
	Mn-Mn	0.8	2.89	0.00763	-2.244	2.878	

Table S2. Areal capacitances of A-MMO, MMO, A-MMO-100, A-MMO-120, A-MMO-160, and A-MMO-25 at various current densities

Samples	2	3	5	10	15	20	30	50	60	Current density (mA cm^{-2})
MnO_2	413	325	227	114	68	45	N	N	N	
Mo-MnO_2	1334	1127	991	791	668	582	422	232	201	
F-MnO_2	1089	1064	1005	909	805	728	628	455	408	
MMO	2084	1966	1860	1535	1394	1244	954	518	360	Capacitance (mF cm^{-2})
A-MnO_2	455	442	435	418	382	364	326	249	216	
A-MMO	2480	2375	2255	2124	1978	1858	1702	1364	1266	
A-MMO-100	2302	2228	2114	1873	1664	1509	1227	847	737	
A-MMO-120	2416	2269	2136	1964	1828	1673	1473	1141	982	
A-MMO-160	2095	2024	1918	1778	1683	1600	1457	1219	1124	
A-MMO-25	3160	2894	2684	2358	2212	1895	1631	1255	1034	

Table S3. Cell parameters of A-MMO during the charging/discharging process.

	a (Å)	b (Å)	c (Å)	Cell volume (Å^3)
C0	5.0435	2.8576	7.3917	102.4945
C0.2	4.9294	2.8561	7.3882	100.2276
C0.4	4.9074	2.8522	7.3657	99.2147
C0.6	4.8110	2.8522	7.3398	96.5144
C0.8	4.7714	2.8522	7.3458	95.7111
C1	4.7260	2.8522	7.3310	94.7309
C1.1	4.7154	2.8456	7.3212	93.8200
D1	4.7436	2.8482	7.3950	95.8380
D0.8	4.8353	2.8495	7.4175	97.7359
D0.6	4.8755	2.8548	7.4154	98.7685
D0.4	4.9275	2.8565	7.4152	100.0625
D0.2	4.9226	2.8561	7.4459	100.4368
D0	4.9713	2.8667	7.4476	102.5243

Table S4. Areal capacitances of N, P-VO_x, N-VO_x, P-VO_x, and V_2O_5 at various current densities

Samples	2	3	5	10	15	20	30	50	60	Current density (mA cm^{-2})
N, P-VO_x	2490	2450	2376	2233	2138	2057	1840	1458	1300	Capacitance ($mF\ cm^{-2}$)
N-VO_x	2057	1421	1200	967	825	750	645	246	525	
P-VO_x	1275	1145	983	783	663	583	475	333	250	
V_2O_5	1156	997	866	643	531	450	350	235	196	

Table S5. Electrochemical performance comparison of A-MMO and N, P-VO_x with other electrodes

Electrodes	Capacitance (F cm^{-2}@mA cm^{-2})	Rate performance (@mA cm^{-2})	Potential window (V)	Cycling performance	Reference
MoS_2@α-Fe_2O_3	2.08@2	85.2%@20	−0.8-0	91.5%@6000 cycles	10
V/Co oxides	1.83@8	40.2%@80	0-0.45	/	11
NiMnLDH	2.11@2	74%@20		93.5%@2000 cycles	12
$CoNiO_2$	1.36@8	83%@100	0-0.45	102%@40000 cycles	13
CoN-Ni_3N	1.48@0.5	41.9%@30	0-0.6	93.3%@10000 cycles	14
Mxene	1.12@10 mV s^{-1}	66%@100 mV s^{-1}	−0.6-0.3	100%@10000 cycles	15
Zinc manganese oxide	1.9@3	55%@50	0-1.2	94.6%@10000 cycles	16
VN	0.63@2	42.3%@50	−1.2-0	95.2%@10000 cycles	17
MnO_2 nanosheets	1.43@1	47.3%@50	0-1	98.4%@50,000 cycles	18
MnO_2@textile	0.53@1	45.1%@50	0-0.8	99.7%@10000 cycles	19
CNT film@MnO_2	1.1@1	63.6%@15	0-1.2	92%@2000 cycles	20
Na-doped MnO_2	0.73@1	71.2%@10	0-1.2	92.1%@5000 cycles	21
VO_x	1.57@2	31.2%@40	0.9-0	no loss@20000 cycles	22
W_2N	0.77@2	63%@20	−0.6-0.6	92%@10000 cycles	23
Ni_3P	1.76@5	63.8%@20	−0.2-0.6	86%@4000 cycles	24
PPy@MnO_2	1.24@2	57.2%@20	0-1	/	25
Co_3O_4	1.22@0.5	59%@20	0-0.5	98.2%@4000 cycles	26
VN	0.72@1	68.8%@10	−1-0.2	/	27
$ZnCo_2O_4$@Zn-Co-S	1.35@0.5	40%@2	0-0.45	/	28
Cu-MOF	0.25@1.25	83.1%@5	0-0.5	87%@4000 cycles	29
N-VO_2	1.013@1 A cm^{-3}	63.8@10 A cm^{-3}	0-0.8	/	30
A-MMO	**2.48@2**	**85.6%@10 74.9%@20 55.0%@50 51.0%@60**	**0-1.1**	**96.0%@10000 cycles**	**This work**
N, P-VO_x	**2.49@2**	**89.7%@10 82.6%@20 58.6%@50 52.2%@60**	**−1.2-0**	**89.5%@10000 cycles**	

Table S6. Electrochemical performance comparison of SCs in this work

SCs	Mass loading of two electrodes in total (mg cm^{-2})	Thickness (mm)	Volumetric energy density (mWh cm^{-3})	Volumetric power density (mW cm^{-3})
A-MMO//N, P-VO_x	12.5	0.8	15.82	29
A-MMO-25//N, P-VO_x-60	18.6	0.9	17.90	26
MMO//N, P-VO_x	13.2	0.9	11.63	26
A-MMO//NG	20.4	1	4.68	23

Table S7. Electrochemical performance comparison of the A-MMO//N, P-VO_x device with other SCs

SCs	Voltage window (V)	Energy density (mWh cm^{-3})	Power density (mW cm^{-3})	Reference
K^+/Na^+ inserted MnO_2//C	2.5	1.43	7.9	31
MnO_x//VO_x	2.2	5	22	32
MnO_2//Fe_2O_3	2	0.64	14.8	33
MnO_2//reduced CC	4	3.82	24.6	34
PPy@MnO_2//Fe_2O_3	2	1.93	9.8	25
$ZnCo_2O_4$//Fe_3O_4	2	2.32	33.3	35
MnO_2//TiO_2	2.6	4.75	13	18
MnO_2//Fe_2O_3	2.1	4.1	22.3	20
MnO_2//VN	2.4	8.3	34.3	17
MnO_2//V_2O_5	2.4	6.24	33	16
symmetric VO_X	1.5	7.7	39	36
W_2N//PPy	1.6	1.9	232	23
$CoNiO_2$//C	1.5	1.4	24	13
CoS_2//C	1.6	3.16	37.3	37
MnO_2//V_2O_5	2	8.25	280	38
symmetric Fe_2O_3	1.8	9.2	12	39
PPy@MnO_2//C	1.8	8.69	12.35	40
NiO_x//FeO_x	1.6	6.19	334.15	41
Ni-Co-N//C	1.5	4.78	150	42
A-MMO//N, P-VO_x	**2.3**	**15.82** **7.57**	**29** **575**	**This work**

Table S8. Electrochemical performance and properties of the A-MMO//N, P-VO_x device with other SCs

Cells	State	Electrolyte	Mass loading of active materials (mg cm^{-2})	Thickness (mm)	Areal energy density (mWh cm^{-2})	Reference
MoS_2//MnO_2	Solid-state SC	PVA/Na_2SO_4	19.7 of MnO_2	/	1.5	[43]
Symmetric graphene	Aqueous SC	6 M KOH	42	1.02 (electrode scale)	0.52	[44]
MnO_2//V_2O_5	Solid-state SC	PVA/Na_2SO_4	21.6	1.04 (device sacle)	0.83	[38]
Symmetric graphene/MnO_2	Aqueous SC	3 M LiCl	364.4	8 (electrode scale)	1.56	[45]
MnO_2//activated carbon	Aqueous SC	1 M Na_2SO_4	105	1 (electrode scale)	1.6	[46]
MnO_2/GA//GA	Aqueous SC	3 M LiCl	31.6	2 (electrode scale)	0.65	[47]
Symmetric $Ti_3C_2T_x$	Aqueous SC	3 M H_2SO_4	32.36	0.7 (electrode scale)	0.337	[48]
MnO_2//carbon	Solid-state SC	PVA/LiCl	33.4	0.9 (device sacle)	0.841	[49]
CNT//CNT/PPy	Solid-state SC	PVA/LiCl	55.1	/	1.42	[50]
A-MMO//N, P-VO_x	**Quasi solid-state SC**	**PVA/Na_2SO_4**	**12.5**	**0.8 (device scale)**	**1.27**	**This work**
A-MMO-25//N, P-VO_x-60	**Quasi solid-state SC**	**PVA/Na_2SO_4**	**18.6**	**1 (device scale)**	**1.61**	

Note: Thickness of the device refers to the total thickness of negative and positive electrodes, separator, and electrolyte.

References

1 B. Ravel and M. Newville, *J. Synchrotron Radiat.*, 2005, **12**, 537–541.

2 X. Gao, X. Dong, Z. Xing, C. Nie, G. Zheng and Z. Ju, *Adv. Mater. Technol.*, 2021, **6**, 2100207.

3 G. Kresse and J. Furthmüller, *Comput. Mater. Sci.*, 1996, **6**, 15–50.

4 G. Kresse and J. Furthmüller, *Phys. Rev. B*, 1996, **54**, 11169.

5 J. P. Perdew, K. Burke and M. Ernzerhof, *Phys. Rev. Lett.*, 1996, **77**, 3865–3868.

6 J. D. Pack and H. J. Monkhorst, *Phys. Rev. B*, 1977, **16**, 1748–1749.

7 L. Zhu, J. Wang, S. Rong, H. Wang and P. Zhang, *Appl. Catal. B Environ.*, 2017, **211**, 212–221.

8 J. Wang, J. Polleux, J. Lim and B. Dunn, *J. Phys. Chem. C*, 2007, **111**, 14925–14931.

9 S. Chen, H. Yu, L. Chen, H. Jiang and C. Li, *Chem. Eng. J.*, 2021, **423**, 130208.

10 P. Man, Q. Zhang, Z. Zhou, M. Chen, J. Yang, Z. Wang, Z. Wang, B. He, Q. Li, W. Gong, W. Lu, Y. Yao and L. Wei, *Adv. Funct. Mater.*, 2020, **30**, 2003967.

11 G. Nie, X. Zhao, J. Jiang, Y. Luan, J. Shi, J. Liu, Z. Kou, J. Wang and Y. Z. Long, *Chem. Eng. J.*, 2020, **402**, 126294.

12 J. Q. Xie, L. Jiang, J. Chen, D. Mao, Y. Ji, X. Z. Fu, R. Sun and C. P. Wong, *Chem. Eng. J.*, 2020, **393**, 124598.

13 R. Guo, J. Li, Y. Jia, F. Xin, J. Sun, L. Dang, Z. Liu and Z. Lei, *J. Mater. Chem. A*, 2019, **7**, 4165–4174.

14 K. Li, B. Zhao, H. Zhang, H. Lv, J. Bai, H. Ma, P. Wang, W. Li, J. Si, X. Zhu and Y. Sun, *Adv. Funct. Mater.*, 2021, **31**, 2103073.

15 Y. Wang, X. Wang, X. Li, X. Li, Y. Liu, Y. Bai, H. Xiao and G. Yuan, *Adv. Funct. Mater.*, 2021, **31**, 2008185.

16 L. Lyu, C. W. Kim, K. dong Seong, J. Kang, S. Liu, Y. Yamauchi and Y. Piao, *Chem. Eng. J.*, 2022, **430**, 133115.

17 G. Qu, Z. Wang, X. Zhang, S. Zhao, C. Wang, G. Zhao, P. Hou and X. Xu, *Chem. Eng. J.*, 2022, **429**, 132406.

18 Y. J. Gu, W. Wen and J. M. Wu, *J. Power Sources*, 2020, **469**, 228425.

19 R. Liu, Y. Wang, G. Yuan, Y. Liu, X. Li, Y. Bai and Y. Wang, *Electrochim. Acta*, 2019, **299**, 12–18.

20 Y. Zhang, X. Yuan, W. Lu, Y. Yan, J. Zhu and T. W. Chou, *Chem. Eng. J.*, 2019, **368**, 525–532.

21 Q. Zong, Q. Zhang, X. Mei, Q. Li, Z. Zhou, D. Li, M. Chen, F. Shi, J. Sun, Y. Yao and Z. Zhang, *ACS Appl. Mater. Interfaces*, 2018, **10**, 37233–37241.

22 K. Zheng, Y. Zeng, S. Liu, C. Zeng, Y. Tong, Z. Zheng, T. Zhu and X. Lu, *Energy Storage Mater.*, 2019, **22**, 410–417.

23 D. P. Dubal, N. R. Chodankar and S. Qiao, *Small*, 2019, **15**, 1804104.

24 P. Sun, M. Qiu, J. Huang, J. Zhao, L. Chen, Y. Fu, G. Cui and Y. Tong, *Chem. Eng. J.*, 2020, **380**, 122621.

25 P. Zhao, N. Wang, M. Yao, H. Ren and W. Hu, *Chem. Eng. J.*, 2020, **380**, 122488.

26 C. Young, J. Wang, J. Kim, Y. Sugahara, J. Henzie and Y. Yamauchi, *Chem. Mater.*, 2018, **30**, 3379–3386.

27 Q. Zhang, X. Wang, Z. Pan, J. Sun, J. Zhao, J. Zhang, C. Zhang, L. Tang, J. Luo, B. Song, Z. Zhang, W. Lu, Q. Li, Y. Zhang and Y. Yao, *Nano Lett.*, 2017, **17**, 2719–2726.

28 J. Zhao, H. Li, C. Li, Q. Zhang, J. Sun, X. Wang, J. Guo, L. Xie, J. Xie, B. He, Z. Zhou, C. Lu, W. Lu, G. Zhu and Y. Yao, *Nano Energy*, 2018, **45**, 420–431.

29 R. Hou, M. Miao, Q. Wang, T. Yue, H. Liu, H. S. Park, K. Qi and B. Y. Xia, *Adv. Energy Mater.*, 2019, **9**, 1901892.

30 J. Guo, L. Li, J. Luo, W. Gong, R. Pan, B. He, S. Xu, M. Liu, Y. Wang, B. Zhang, C. Wang, L. Wei, Q. Zhang and Q. Li, *Adv. Energy Mater.*, 2022, **12**, 2201481.

31 Y. Liu, L. Guo, X. Teng, J. Wang, T. Hao, X. He and Z. Chen, *Electrochim. Acta*, 2019, **300**, 9–17.

32 Y. Song, T. Liu, B. Yao, M. Li, T. Kou, Z. H. Huang, D. Y. Feng, F. Wang, Y. Tong, X. X. Liu and Y. Li, *ACS Energy Lett.*, 2017, **2**, 1752–1759.

33 D. Chen, S. Zhou, H. Quan, R. Zou, W. Gao, X. Luo and L. Guo, *Chem. Eng. J.*, 2018, **341**, 102–111.

34 J. Zhang, J. Sun, T. Ahmed Shifa, D. Wang, X. Wu and Y. Cui, *Chem. Eng. J.*, 2019, **372**, 1047–1055.

35 D. Kong, Y. Wang, S. Huang, J. Hu, Y. Von Lim, B. Liu, S. Fan, Y. Shi and H. Y. Yang, *Energy Storage Mater.*, 2019, **23**, 653–663.

36 A. Huang, M. F. El-Kady, X. Chang, M. Anderson, C. W. Lin, C. L. Turner and R. B. Kaner, *Adv. Energy Mater.*, 2021, **11**, 2100768.

37 W. Chen, T. Wei, L. E. Mo, S. Wu, Z. Li, S. Chen, X. Zhang and L. Hu, *Chem. Eng. J.*, 2020, **400**, 125856.

38 Z. H. Huang, Y. Song, D. Y. Feng, Z. Sun, X. Sun and X. X. Liu, *ACS Nano*, 2018, **12**, 3557–3567.

39 J. Li, Y. Wang, W. Xu, Y. Wang, B. Zhang, S. Luo, X. Zhou, C. Zhang, X. Gu and C. Hu, *Nano Energy*, 2019, **57**, 379–387.

40 J. Tao, N. Liu, L. Li, J. Su and Y. Gao, *Nanoscale*, 2014, **6**, 2922–2928.

41 Y. Wang, S. Su, L. Cai, B. Qiu, C. Yang, X. Tao and Y. Chai, *Energy Storage Mater.*, 2019, **20**, 315–323.

42 F. Liu, L. Zeng, Y. Chen, R. Zhang, R. Yang, J. Pang, L. Ding, H. Liu and W. Zhou, *Nano Energy*, 2019, **61**, 18–26.

43 J. M. Jeong, S. H. Park, H. J. Park, S. Bin Jin, S. G. Son, J. M. Moon, H. Suh and B. G. Choi, *Adv. Funct. Mater.*, 2021, **31**, 2009632.

44 L. Sheng, J. Chang, L. Jiang, Z. Jiang, Z. Liu, T. Wei and Z. Fan, *Adv. Funct. Mater.*, 2018, **28**,

1800597.

45 B. Yao, S. Chandrasekaran, J. Zhang, W. Xiao, F. Qian, C. Zhu, E. B. Duoss, C. M. Spadaccini, M. A. Worsley and Y. Li, *Joule*, 2019, **3**, 459–470.

46 C. Chen, Y. Zhang, Y. Li, J. Dai, J. Song, Y. Yao, Y. Gong, I. Kierzewski, J. Xie and L. Hu, *Energy Environ. Sci.*, 2017, **10**, 538–545.

47 B. Yao, S. Chandrasekaran, H. Zhang, A. Ma, J. Kang, L. Zhang, X. Lu, F. Qian, C. Zhu, E. B. Duoss, C. M. Spadaccini, M. A. Worsley and Y. Li, *Adv. Mater.*, 2020, **32**, 1906652.

48 J. Kong, H. Yang, X. Guo, S. Yang, Z. Huang, X. Lu, Z. Bo, J. Yan, K. Cen and K. K. Ostrikov, *ACS Energy Lett.*, 2020, **5**, 2266–2274.

49 H. Wang, C. Xu, Y. Chen and Y. Wang, *Energy Storage Mater.*, 2017, **8**, 127–133.

50 R. Chen, H. Ling, Q. Huang, Y. Yang and X. Wang, *Small*, 2022, **18**, 2106356.